# Comparison of Gravity Current Mixing Parameterizations and Calibration Using a High-Resolution 3D Nonhydrostatic Spectral Element Model

by

Yeon S. Chang[1], Xiaobiao Xu[1], Tamay M. Özgökmen[1],

Eric P. Chassignet[1], Hartmut Peters[1] and Paul F. Fischer[2]

1. RSMAS/MPO, University of Miami, Miami, Florida
2. Mathematics and Computer Science Division, Argonne National Laboratory

   Argonne, Illinois

Accepted for publication in:

*Ocean Modelling*

November 8, 2004

## Abstract

In light of the pressing need for development and testing of reliable parameterizations of gravity current entrainment in ocean general circulation models, two existing entrainment parameterization schemes, K-Profile Parameterization (KPP) and one based on Turner's work (TP), are compared using idealized experiments of dense water flow over a constant-slope wedge using the HYbrid Coordinate Ocean Model (HYCOM). It is found that the gravity current entrainment resulting from KPP and TP differ significantly from one another. Parameters of KPP and TP are then calibrated using results from the high-order nonhydrostatic spectral element model Nek5000. It is shown that a very good agreement can be reached between the HYCOM simulations with KPP and TP, even though these schemes are quite different from each other.

## 1. Introduction

Most deep and intermediate water masses of the world ocean are released into the large-scale circulation from high-latitude and marginal seas in the form of overflows. For reasons of mass conservation, this downward transport implies upwelling elsewhere in the ocean, and the resulting overturning circulation affects the large-scale horizontal flow through the stretching term in the vorticity balance (e.g., Gargett, 1984). Model representations of overflows thus determine more than just the properties of intermediate and deep water masses in the ocean. With this background, it is easy to comprehend why ocean general circulation models (OGCMs) are highly sensitive to detail of the representation of overflows in these models (e.g., Willebrand et al., 2001). Specifically, the entrainment of ambient waters into overflows is a prominent oceanic processes with significant impact on the ocean general circulation, and the climate in general.

Parameterizing the gravity current entrainment in coarse-resolution OGCMs has proven to be challenging. Recent simulations of the Mediterranean overflow employing isopycnic coordinates (Papadakis et al., 2003) and terrain-following coordinates (Jungclaus and Mellor, 2000) appear promising, while the representation of continuous slopes as steps in geopotential vertical coordinate models remains a daunting problem (e.g., Beckmann and Döscher, 1997; Winton et al., 1998; Killworth and Edwards, 1999; Nakano and Suginohara, 2002).

In this paper we exclusively focus on entrainment parameterization in isopycnic coordinate models. Isopycnic models have a vertical resolution that naturally migrates to the density front atop the gravity current, and the amount of diapycnal mixing can be exactly prescribed (i.e., no numerically-induced diapycnal mixing takes place as in geopotential coordinate models, e.g., Griffies et al. 2000). We conduct and analyze a series of numerical simulations of overflows by employing parameterizations of the entrainment simple enough to be used in coarse-resolution climate models integrated over long time periods. Our choice of parameterization is pragmatic, motivated by frequent current use in OGCMs. Wanting to examine simple parameterizations first, we deliberately ignore the more complex, and computationally-expensive schemes, such as two-equation turbulence closures, applications to overflows being those of Jungclaus and Mellor (2000), and Ezer and Mellor (2004).

One of the schemes examined herein is the K-Profile Parameterization, KPP (Large et al., 1994, 1999). Its non-local treatment of convection plays no role in overflows, and for our purposes, KPP is basically a modification of the recipes of Pacanowski and Philander (1981) and Munk and Anderson (1948), the latter ultimately going back to observations taken about a century ago and analyzed by Jacobsen (1913). In these recipes, eddy viscosity and eddy diffusivity are specified as a dimensional constant times a simple analytical function of the gradient Richardson number. The constant is the maximum possible eddy coefficient. Accordingly, the scheme cannot possibly be universally valid.

The other parameterization, henceforth referred to as TP, was adopted by Hallberg (2000) from the laboratory experiments of Turner (1986) and Ellison and Turner (1959). Their original work contains an analysis of the entrainment velocity into gravity currents as function of the bulk Richardson number of this current. Ingeneously, Hallberg simply translated the bulk Richardson number into a gradient Richardson number ($Ri$). Rather than prescribing eddy coefficients as in KPP, TP thus prescribes the net entrainment velocity into a layer as the velocity difference across the layer times an analytical function of the gradient Richardson number. Unlike KPP, TP is hence proportional to the forcing by the shear. TP has been implemented and tested in two isopycnic OGCMs, HIM (Hallberg Isopycnic coordinate ocean Model; Hallberg, 2000) and MICOM (Miami Isopycnic Coordinate Ocean Model; Papadakis et al., 2003).

The evaluation of the realism of mixing parameterizations in OGCMs obviously requires some ground truth. In this paper, we bypass the commonly significant difficulties of comparing models to field observations by taking the recent three-dimensional (3D) high-resolution nonhydrostatic simulations of a generic overflow by Özgökmen et al. (2004a) as our ground truth. This model resolves the largest turbulent eddies, and, being nonhydrostatic, is physically quite complete. Results from this high-resolution, nonydrostatic simulations are compared to those from a hydrostatic, layered OGCM such that the validity of the parameterization schemes can be examined. Our approach is as follows: by comparing the results from nonhydrostatic model to those from OGCM, we quantify the differences and limitations of the two examined Richardson number-dependent parameterizations, understand why and how these parameterizations can be modified to produce consistent results. Finally, we discuss remaining problems with both schemes.

The paper is organized as follows. Relevant background information is given in section 2. In section 3, the details of the mixing parameterizations KPP and TP are introduced. The nonhydrostatic model and the hydrostatic OGCM are introduced in section 4 along with the experimental setup, and the model parameters are discussed. The results are presented in section 5. Finally, the principal findingss are discussed, and future directions are summarized in section 6.

## 2. Background

A few additional remarks on the physics of overflows and their past analyses as well as on the models employed herein facilitate the understanding of this paper. The seminal investigations by Price et al. (1993, 1994) reveal that the mixing of overflows with the ambient fluid takes place over very small spatial and time scales. Results from observational programs in the Mediterranean Sea overflow (Baringer and Price, 1997a,b), Denmark Strait overflow (Girton et al., 2001; 2003), Red Sea overflow (Peters et al., 2004a,b), Faroe Bank Channel (Price, 2004) and Antarctic Ocean (Gordon et al., 2004) demonstrate the importance of small-scale mixing processes in the dynamics of overflows, and frequently show a high variability of overflow properties in time and space. Detailed, quantitative field observations of the turbulent mixing in overflows are still few (Johnson et al., 1994a,b; Peters and Johns, 2004).

Hence, much of our present understanding of such mixing is derived from laboratory tank experiments (Ellison and Turner, 1959; Simpson, 1969; Britter and Linden, 1980; Simpson, 1982; Turner, 1986; Simpson, 1987; Hallworth et al., 1996; Monaghan et al., 1999; Baines, 2001; Cenedese and Whitehead, 2004). However, when configured for the small slopes of observed overflows [$< 2^o$], the dense source fluid cannot accelerate enough within the bounds of typical laboratory tanks [$O(1\,\mathrm{m})$] to produce turbulent behavior. For turbulence to occur, laboratory experiments are configured with slopes greater than $10^o$. It is further difficult to maintain a complex ambient stratification in these tanks. Ellison and Turner (1959) and Turner (1986) parameterized the entrainment rates observed in their tank experiments as functions of bulk Richardson numbers of the flow. Their approach formed the basis for Hallberg's (2000) TP parameterization. The original Turner parameterization has been employed in so-called stream tube models, which have proven to be useful in examining the path and bulk properties of the Denmark Strait overflow (e.g., Smith, 1975), Weddell Sea overflow (Killworth, 1977), the Mediterranean overflow (Baringer and Price, 1997b) and Red Sea and Persian Gulf overflows (Bower et al., 2000).

With the recent advances in numerical techniques and computer power, numerical modeling provides an alternative avenue to investigate these processes. Nonhydrostatic, high-resolution, two-dimensional simulations of bottom gravity currents conducted by Özgökmen and Chassignet (2002) capture explicitly the major features of these currents seen in laboratory experiments, such as the presence of a head in the leading edge and Kelvin-Helmholtz vortices in the trailing fluid. Subsequently, this model was used to simulate the part of the Red Sea outflow in a submarine canyon, which naturally restricts motion in the lateral direction such that the use of a two-dimensional (2D) model provides a reasonable approximation to the dynamics. It was shown (Özgökmen et al., 2003) that this model adequately captures the general characteristics of mixing in the Red Sea overflow within the limitations of a 2D model. These limitations include lack of edge effects or intrusions from channel walls associated with the span wise structure. Recently, a parallel high-order spectral element Navier-Stokes solver, Nek5000, developed by Fischer (1997), was used to conduct nonhydrostatic 3D simulations of bottom gravity currents (Özgökmen et al., 2004a,b).

In this study, our objective is to explore how mixing parameterizations perform in an idealized setting that represents the very basics of shear-induced mixing in bottom gravity currents, e.g. flow of a dense water mass released at the top of a sloping wedge. To this end, we conduct experiments with a layered hydrostatic OGCM, HYCOM (HYbrid Coordinate Ocean Model), employing KPP and TP, and compare the results to those from high-resolution 3D nonhydrostatic simulations by Özgökmen et al. (2004a). We start out from the questions (a) how the results from KPP and TP compare to each other and to those from the 3D nonhydrostatic simulations, and (b) how the results change and/or converge as a function of the grid spacing. Discussing our results, we examine what the principal limitations of the KPP and TP parameterizations are and how can they be developed into a consistent formulation for use in layered ocean models.

## 3. Mixing parameterizations

### 3.1. KPP

The K-Profile Parameterization (Large et al., 1994, 1999; KPP) provides a prescription for mixing from surface to bottom, smoothly matching large values of the eddy diffusivity ($K$) in the surface boundary layer to small values in the interior of the ocean. KPP has been popular because it includes prescriptions for a fairly wide range of physical processes, shear-driven mixing in low-$Ri$ regions, constant background internal-waves induced mixing allowing counter-gradient fluxes. Herein, only the shear-induced mixing is important, a component of KPP that was not specifically tailored to gravity currents. Shear-driven mixing is expressed in terms of the gradient Richardson number $Ri$ calculated at layer interfaces:

$$Ri \quad = \quad N^2 \left[ (\frac{\partial \bar{u}}{\partial z})^2 + (\frac{\partial \bar{v}}{\partial z})^2 \right]^{-1} , \tag{1}$$

where the numerator is the buoyancy frequency, $N^2 = -\frac{g}{\rho_0}\frac{\partial \rho}{\partial z}$, written here for an incompressible fluid for simplicity, and where $g = 9.81\,\mathrm{m}^2\mathrm{s}^{-1}$ is the gravitational acceleration. The denominator in (1) is the vertical shear. The vertical diffusivity is then related to $Ri$ as

$$K_{shear} \quad = \quad K_{max} \times \left[ 1 - min(1\,,\,(\frac{Ri}{Ri_c}))^2 \right]^3 \tag{2}$$

so that vertical diffusivity is zero when $Ri \geq Ri_c$ corresponding to the case in which stratification overcomes the effect of vertical shear and prohibits vertical mixing (Fig. 1a). In this case, mixing can only take place in the horizontal plane, or as so-called "pancake" mixing demonstrated in laboratory experiments of stratified flow (e.g., Fernando, 2000). $Ri_c$ is set to $Ri_c = 0.7$.

With decreasing $Ri < Ri_c$, the vertical diffusivity coefficient gradually increases to account for mixing induced by high vertical shear and/or weaker stratification. At the limit of $Ri = 0$, mixing takes place as in homogeneous (unstratified) fluid. The concept behind this component of KPP is taken from Pacanowski and Philander (1981), but the shape of the mixing curve in KPP was adjusted to show better agreement with observational results from equatorial mixing by Gregg et al. (1985) and Peters et al. (1988) for the regime of $0.3 \leq Ri \leq 0.7$. The diffusivity value at $Ri = 0$ was determined from large eddy simulation (LES) studies of the upper tropical ocean as $K_{max} = 50\, cm^2\, s^{-1}$ (e.g., Large, 1998).

The boundary shear stress component of KPP can be invoked to account for the bottom stress in the bottom boundary layer (BBL):

$$K_{shear} = h_b\, w_S\, G_S\ . \tag{3}$$

Here, $h_b$ is the bottom boundary layer thickness, estimated as the total thickness of layers, counted from the bottom, in which the Richardson number remains lower than the critical value. The velocity scale $w_S$ is a linear function of the friction velocity which is proportional to the square root of the bottom stress $\rho c_d |\mathbf{u_b}| \mathbf{u_b}$, where $c_d = 3 \times 10^{-3}$ and $\mathbf{u}_b$ is the bottom velocity. $G_S$ is a third-order smooth shape function to match with the interior profiles. The reader is referred to Large et al. (1994) for further detail on KPP, and to Halliwell (2004) on the numerical implementation of KPP in HYCOM.

### 3.2. TP

Based on the results and parameterization by Turner (1986) and Ellison and Turner (1959), Hallberg (2000) developed a mixing parameterization, in which the net entrainment velocity into layers in gravity currents $w_E$ is expressed as

$$w_E = \begin{cases} C_A \Delta U (0.08 - 0.1 Ri)/(1 + 5 Ri) & \text{if } Ri < 0.8 \\ 0 & \text{if } Ri \geq 0.8\ , \end{cases} \tag{4}$$

where $\Delta U$ is the mean velocity difference across layers, $C_A = 1$ is a proportionality constant, and the cut-off Richardson number is $Ri_c = 0.8$. The reader is referred to Hallberg (2000) for further detail of the numerical implementation.

Because both TP and KPP employ functions of $Ri$, there is similarity between the prescriptions of shear-driven mixing in TP (4) and KPP (2). Fig. 1a,b depicts the different shapes of the mixing curves and the different values of the critical $Ri$. An important difference lies in the hard limit $K \leq K_{max}$ in KPP and the absence of any such limit in TP.

## 4. The numerical models and experimental configuration

### 4.1. Nonhydrostatic 3D model Nek5000:

Results from the high-order parallel spectral element Navier Stokes solver, Nek5000, are used as a reference. This model is documented in detail by Fischer (1997), Fischer et al. (2000), Tufo and Fischer (1999), and Fischer and Mullen (2001). A short description of the model in the context of bottom gravity current experiments can also be found in Özgökmen et al. (2004a).

Nek5000 is a state-of-the-art general computational fluid dynamics code (see http://www-unix.mcs.anl.gov/~fischer/ for applications) that is based on the spectral element method (SEM), and offers several fundamental advantages with respect to the more common numerical discretization techniques (finite-difference, finite-element, finite-volume and spectral); (a) SEM combines the geometrical flexibility of finite element method with the numerical accuracy of spectral expansion (e.g., the geometrical flexibility of SEM has been exploited to explore the behavior of bottom gravity currents over complex topography in Özgökmen et al. 2004b); (b) SEM has minimal dissipation and dispersion errors, which are important in problems involving propagation of high gradients and mixing, such as in the present problem; (c) SEM provides dual path to convergence, either via elemental grid refinement or by increasing the polynomial degree; (d) SEM offers computational advantages for scalability on parallel computers (Tufo and Fischer, 1999).

In the present setup, Nek5000 is configured to solve the Boussinesq equations:

$$\frac{D\mathbf{u}}{Dt} = -\nabla p + \nabla_r^2 \mathbf{u} - Ra\, S\, \hat{\mathbf{z}} \,, \tag{5}$$

$$\nabla \cdot \mathbf{u} = 0 \,, \tag{6}$$

$$\frac{DS}{Dt} = Pr^{-1}\, \nabla_r^2 S \,, \tag{7}$$

where the material (total) derivative is $\frac{D}{Dt} := \frac{\partial}{\partial t} + \mathbf{u} \cdot \nabla$, and the anisotropic diffusivity is

$$\nabla_r^2 \quad := \quad \frac{\partial^2}{\partial x^2} + \frac{\partial^2}{\partial y^2} + r\frac{\partial^2}{\partial z^2} \,. \tag{8}$$

The variables are the velocity vector field $\mathbf{u} = (u, v, w)$ and the pressure $p$, and the nondimensional parameters are $Ra = (g\,\beta\,\Delta S\,H^3)/\nu_h^2$ the Rayleigh number, the ratio of the strengths of buoyancy and viscous forces, where $H$ is the domain depth and $\Delta S$ is the salinity range in the system, $\beta = 7 \times 10^{-4}\,\mathrm{psu}^{-1}$ is the salinity contraction coefficient (a linear equation of state is used); $Pr = \nu_h/K_h$ the Prandtl number, the ratio of viscous and saline diffusion; and $r = \nu_v/\nu_h = K_v/K_h$, the ratio of vertical and horizontal diffusivities.

### 4.2. Hydrostatic ocean model HYCOM:

The development of Hybrid Coordinate Ocean Model (HYCOM) was motivated by the fact that no single vertical coordinate - depth, density, or terrain-following - can be by itself optimal everywhere in the ocean. The default configuration in HYCOM is one that is isopycnal in the open stratified ocean but smoothly reverts to a terrain-following coordinate in shallow coastal regions and to fixed pressure-level coordinates in the surface mixed layer and unstratified seas. In doing so, the model ideally combines the advantages of the different types of coordinates in simulating coastal and open ocean circulation features. The basic principles of this generalized vertical coordinate model are described in Bleck (2002), Chassignet et al. (2003), and Halliwell (2004), and detailed documentation is readily available from http://hycom.rsmas.miami.edu.

### 4.3. Experimental configuration:

In Nek5000, the model domain has a horizontal (stream wise) length of $L_x = 10$ km and a span wise width of $L_y = 2$ km. The depth of the water column ranges from 400 m at $x = 0$ to $H = 1000$ m at $x = 10$ km, hence the background slope angle is $\theta = 3.5°$ (Fig. 2a). The boundary conditions at the bottom are no-slip and no-normal flow for the velocity components, and no-normal flux, $\partial S/\partial \mathbf{n} = 0$, with $\mathbf{n}$ being the normal direction to the boundary, for salinity. Rigid-lid and free-slip boundary conditions are used at the top boundary. The model is driven by the velocity and salinity forcing profiles at the inlet boundary at $x = 0$. The model is initialized by using a salinity distribution of the (dimensional) form

$$S(x,y,z,t=0) = \frac{\Delta S}{2} \exp\left( - \left\{ \frac{x}{L_x \left(1 + 0.1 \sin(\pi \frac{y}{H})\right)} \right\}^{20} \right) \left[ 1 - \cos\left( \pi \frac{H-z}{0.4H} \right) \right] \; .$$

The sinusoidal perturbation in the spanwise direction facilitates the transition to 3D flow. A section of the initial salinity profile across the middle of the domain (Fig. 2b) shows that the initial thickness of the dense water mass is $h_0 = 200$ m. The velocity distribution at the inlet matches no-slip at the bottom and free-slip at the top in such a way that the depth-integrated mass flux across this boundary is zero. The amplitude of the inflow velocity profile scales with the propagation speed of the gravity current, which is zero at $t = 0$ and reaches a constant value $U_F$ shortly after its release such that the bulk Froude number is near critical, $Fr \equiv U_F/\sqrt{g\beta\Delta S\, h_0} \approx 0.9$, which is characteristic for overflows emanating from narrow straits (e.g., Price et al., 1994; Murray and Johns, 1997). As the interior is initialized with homogeneous, light ($S = 0$) water, the density front propagation is the fastest signal in the system. Density currents reach the exit boundary after about 10,000 s, at which point the integrations are terminated such that potential complications involving the outflow boundary are avoided, albeit with the limitation of focusing only on the start-up phase of plumes rather than those in a statistically steady state. Finally, periodic boundary conditions are applied at the lateral boundary. The domain is discretized using 4000 elements with 10th-order polynomials in each spatial direction within the elements, hence a total of $4 \times 10^6$ grid points are employed. The remaining model parameters are listed in Table 1 and the reader is referred to Özgökmen et al. (2004a) for more detailed discussion. The calculations were carried out on a Linux cluster running on 32 Athlon 1.7 GHz processors, and it takes approximately 9 days to complete (simulated to real-time ratio of $\approx 1/60$).

In HYCOM experiments, the model parameters and the physical conditions of the model are set as closely as possible to those in Nek5000 for the comparison. Two major changes are made in the domain configuration of HYCOM experiments. First, the sloping portion of the domain is extended from 10 km to 20 km (while keeping $\theta = 3.5°$) in order to obtain more reliable estimates of the entrainment parameters (Fig. 3a). Second, an inlet system is designed using a reservoir of 10 km length, initially filled with dense water (Fig. 3b). Shortly after the dam break (at $t = 15$ mins, Fig. 3c), the system becomes nearly equivalent to the initial conditions used in Nek5000 (Fig. 1b) without the use of velocity boundary conditions, and in a fashion consistent with changes in grid spacing. The reservoir contains an adequate amount of dense water for the sloping portion of the domain. Free surface boundary conditions are used at the top boundary, and a quadratic drag law with a drag coefficient of $c_d = 3 \times 10^{-3}$ is applied at the bottom. Free-slip boundary conditions are applied at the lateral boundaries.

One of the objectives of the present study is to explore the behavior of gravity current simulations in HYCOM as a function of grid spacing. Five different horizontal resolutions are used: $\Delta x = \Delta y = 1000, 500, 100, 50,$ and 20 m. The gradual strengthening of nonhydrostatic effects limited the minimum grid spacing to $\Delta x = 20$ m. The horizontal viscosity changes in HYCOM in proportion to grid spacing as $\nu = max \left\{ u_d \, \Delta x, \left[ \left( \frac{\partial u}{\partial x} - \frac{\partial v}{\partial y} \right)^2 + \left( \frac{\partial v}{\partial x} + \frac{\partial u}{\partial y} \right)^2 \right]^{1/2} \Delta x^2 \right\}$, where $u_d = 2 \, cm \, s^{-1}$. Finally, experiments were conducted for both 5 and 11 layers, but since there was no significant difference, we only present results from the 5-layer runs in the following. The main parameters for HYCOM experiments are summarized in Table 2.

One important factor in the dynamics of oceanic overflows is rotation. The scale at which the Coriolis force becomes comparable to the buoyancy force is a complex function of the slope angle, stratification, and friction (e.g., Griffiths, 1986). A simple spatial scale for rotational effects to become important is given by the radius of deformation $\sqrt{g'h}/f$, which, with the stated experimental parameters, is approximately 17 km at midlatitude, as compared to domain lengths of 10 or 20 km. The rotation time scale is $f^{-1} \approx 15000$ s, while, as shown below, the gravity currents cross the domain in $\approx 10000$ or 20000 s. Hence, the results presented here apply to the phase before the impact of rotation starts influencing the flow patterns.

Given that in some overflows the bulk of the entrainment takes place over a very small distance (e.g., over a distance of approximately 40–50 km in the Mediterranean Sea overflow according to Figure 7a of Baringer and Price, 1997b), in the high-resolution studies of Özgökmen and Chassignet (2002), Özgökmen et al. (2003) and Özgökmen et al. (2004a,b) it was considered important that the detail of such entrainment be captured. In this sense this study complements other process studies focusing on the larger-scale behavior (e.g., Ezer and Mellor, 2004).

## 5. Results

### 5.1. Description:

The evolution of the salinity distribution in the Nek5000-experiments is shown in Fig. 4. The system is initialized as described in section 4.3. The initial development of the system is that of the so-called lock-exchange flow (e.g., Keulegan, 1958; Simpson, 1987), in which the lighter fluid remains on top and the denser overflow propagates downslope. The dense gravity current quickly develops a characteristic "head" at the leading edge of the current (Fig. 4b). The head is half of a dipolar vortex, which is a generic flow pattern that tends to form in two-dimensional systems by self-organization of the flow (e.g., Flierl et al., 1981; Nielsen and Rasmussen, 1996), and which corresponds to the most probable equilibrium state maximizing entropy (Smith, 1991). The head grows and is diluted as the gravity current travels further down the slope, the result of entrainment of fresh ambient fluid. The flow along the leading edge of the current is composed of a complex pattern of so-called lobes and clefts that are highly unsteady (Fig. 4c,d) and well-known features from laboratory experiments tracing back to the work of Simpson (1972). It was conjectured, e.g.,by Simpson (1987) that a gravitational rise of the thin layer of light fluid which the gravity current overruns is responsible for the breakdown of the flow at the leading edge. Recently, Härtel et al. (2000) put forth that instability associated with the unstable stratification prevailing at the leading edge between the nose and stagnation point of the front could also account for this behavior.

In the trailing fluid, the initial instabilities appear to be 2D Kelvin-Helmholtz rolls that span the entire width of the domain (Fig. 4c). These rolls gradually exhibit transition to 3D (Fig. 4d). The development of spanwise instabilities in Kelvin-Helmholtz rolls was investigated by Klaassen and Peltier (1991), who classified them into two categories. The first are dynamical secondary instabilities that tend to initiate in the vortex core and the interface between strongly rotational and weakly rotational fluid and that develop independently at different growth rates. The second category are convective secondary instabilities in the statically unstable regions, which develop as the interface between the two streams overturns. Because of these instabilities, Kelvin-Helmholtz billows cannot preserve their coherence in the lateral $y$-direction, and break down. In contrast, Kelvin-Helmholtz billows in 2D can grow by pairing (e.g., Corcos and Sherman, 1984). Therefore, Kelvin-Helmholtz billows in

3D result in smaller coherent overturning structures than those in 2D, and consequently, the entrainment parameter in 3D simulations was found to be smaller than that in 2D (Özgökmen et al., 2004a). Finally, a span-wise averaged salinity distribution is depicted in Fig. 5 for a visual comparison to results from HYCOM experiments.

In HYCOM experiments, mixing of the bottom gravity current with the ambient fluid entirely depends on the mixing parameterizations, in the absence of which, none would occur by design. Results using KPP and TP at coarse resolution of $\Delta x = 1000$ m are illustrated in Fig. 6. At $t = 4950$ s (Fig. 6a, corresponding approximately to Fig. 4c; note that in HYCOM the sloping part of the domain is twice as long as that in Nek5000), there is formation of a characteristic head using KPP. The head grows in time and breaks into two parts before the gravity current reaches the end of the domain at $t = 13050$ s (Fig. 6b,c). In contrast, the growth of the head is nearly absent in the experiment with TP (Fig. 6d,e,f). Clearly, there is significantly more entrainment and dilution of the gravity current resulting in a much slower propagation speed of the gravity current in the experiment with TP than that with KPP. There is no significant variation in $y$-direction in either experiment so that they are effectively 2D, as are the geometry, forcing and initial conditions.

Results from KPP and TP at fine resolution of $\Delta x = 20$ m are shown in Fig. 7. At this resolution, KPP results in a great deal of fine-scale structure in the tail of the gravity current. As shown by Gallacher and Piacsek (2004), this fine-scale behavior occurs because of the hydrostatic approximation, which is shown to lead to unphysical noise related to the overestimation of the vertical velocity at high horizontal resolution. (This noise is more significant in KPP than in TP, but both cases are unstable for $\Delta x \leq 10\,m$.) TP at this resolution yields a head at the leading edge, which is smaller than that in KPP. The main result remains the same in general; there appears to be a significant difference in entrainment resulting from these two schemes in that TP results into substantially more entrainment than KPP.

It is also well-known that bottom gravity currents propagate with a constant speed provided that the input flux is constant. In this flow the gravitational force is balanced by a combination of bottom friction and entrainment (e.g., Britter and Linden, 1980). Fig. 8 shows the position of the density front as a function of time, $X_F(t)$, in experiments with KPP and TP. In all experiments, the speed of propagation, $U_F = dX_F(t)/dt$, is approximately constant. When scaled with the speed of long internal waves, $\sqrt{g'h_0} = 1.18\, ms^{-1}$, where $g' = g\,\beta\,\Delta S \approx 7 \times 10^{-3}\, ms^{-2}$ and $h_0 = 200\, m$, $U_F/\sqrt{g'h_0} = 0.92$ in the case of TP, and $U_F/\sqrt{g'h_0} = 1.23$ in the case of KPP in coarse resolution ($\Delta x = 1000\, m$) experiments. This difference in propagation speed further emphasizes the difference in total entrainment from TP and KPP schemes.

### 5.2. Entrainment:

Turner (1986) defined an entrainment parameter in bottom gravity currents as the change of the dense flow thickness $h$ along the streamwise direction $X$,

$$E \equiv \frac{dh}{dX}\,, \tag{9}$$

a 2D expression, which can be mapped to 3D flows as (Özgökmen et al., 2004a),

$$E(t) \equiv \frac{\overline{h}(t) - \overline{h}_0(t)}{\overline{\ell}(t)}\,, \tag{10}$$

where $\overline{\ell}(t) = L_y^{-1} \int_0^{L_y} X_F(y', t)\, dy' - x_0$ is the spanwise-averaged length of the dense overflow measured between the reference station $x_0$ and the leading edge $X_F(y, t)$, $\overline{h}(t)$ is the total (with entrainment) mean thickness estimated from

$$\overline{h}(t) \equiv \frac{1}{\overline{\ell}(t)\, L_y} \int_0^{L_y} \int_{x_0}^{X_F(y',t)} h(x', y', t)\, dx'\, dy'\,, \tag{11}$$

between a reference station of $x_0$ and the leading edge of the density current $X_F$. The overflow thickness $h$ is calculated from

$$h(x, y, t) \equiv \int_0^{z^b} \delta(x, y, z', t)\, dz' \quad \text{where} \quad \delta(x, y, z, t) = \begin{cases} 0, \text{ when } S(x, y, z, t) < \epsilon \\ 1, \text{ when } S(x, y, z, t) \geq \epsilon \end{cases}\,. \tag{12}$$

The salinity interface threshold value is taken as $\epsilon = 0.2\,(psu)$, since in the case of Nek5000, it is the lowest salinity value remaining as a coherent part of the gravity current (fluid particles with lower salinity tend to detach from the current and be advected with the overlying counter flow). Finally, $\overline{h}_0(t)$ is the original (without any entrainment) mean thickness estimated from

$$\overline{h}_0(t) \equiv \frac{1}{\overline{\ell}(t)\, L_y} \int_0^{t} \int_0^{L_y} \int_{z^b+h}^{z^b} u(x_0, y', z', t')\, dz'\, dy'\, dt'\,. \tag{13}$$

As $E(t)$ accounts for the mixing process of the gravity current with the ambient flows, the comparison of $E(t)$ between the results from HYCOM and Nek5000 can diagnose the appropriateness of the vertical mixing parameters in the hydrostatic ocean models. In Özgökmen et al. (2004a), it was found that the entrainment parameter converges to $E \approx 4 \times 10^{-3}$ in 3D experiments, whereas $E \approx 9 \times 10^{-3}$ in 2D, because of the differences between 2D and 3D turbulence discussed above. These results are plotted in Fig. 9 in comparison to HYCOM experiments with KPP and TP carried out using five different horizontal grid resolutions. Fig. 9a illustrates that the entrainment parameter of KPP converges to a mean value of $E \approx 1 \times 10^{-3}$, which is a significantly less than the value obtained from Nek5000. This result is reasonably independent of the horizontal grid scale; while some oscillatory behavior is evident with $\Delta x = 1000$ m, and some underestimate is obtained with $\Delta x = 500$ m, the entrainment profiles are very similar with the resolutions of 100, 50, and 20 m.

In contrast, $E(t)$ obtained from HYCOM with TP converges to $E \approx 8.5 \times 10^{-3}$ (Fig. 9b), which is in very good agreement with the estimate given by Turner as $E = (5 + \theta) \times 10^{-3}$ for $\theta = 3.5°$. While this entrainment parameter is in approximate agreement with the 2D results from Nek5000, it is larger by a factor of 2 than the value from the 3D simulations. Similar behavior to KPP with regard to the grid scale applies to TP as well; oscillatory convergence is displayed with $\Delta x = 1000$ m, slight underestimation of $E$ results from $\Delta x = 500$ m, and nearly-identical results are obtained with $\Delta x = 100$, $\Delta x = 50$, and $\Delta x = 20$ m. By conducting experiments both with $\Delta t = 9\,s$ and with $\Delta t = 1\,s$, it is found that the oscillatory convergence of $E(t)$ at $\Delta x = 1000$ m is entirely related to spatial discretization.

### 5.3. Calibration of KPP and TP using Nek5000:

The computations discussed in section 5.2 clearly illustrate that, with their original parameters, KPP and TP lead to significantly different results. Further evidence why these parameters should be considered tunable and why there is merit in considering a calibration of the parameters of both KPP and TP relative to results from Nek5000 runs is provided in the summary section further below.

Both KPP and TP have two parameters, the critical gradient Richardson number, above which turbulent mixing terminates, and an amplitude parameter. We have not found significant deviations from the results shown in Fig. 9a,b when $Ri_c$ is changed by $\pm 50\%$. However, varying the respective amplitude parameters in TP and KPP causes large variations in model outputs. Fig. 10 shows the results obtained by adjusting the coefficients $K_{max}$ and $C_A$ in KPP and TP, respectively, such that $E(t)$ approximately matches that obtained from 3D Nek5000 experiments. Specifically, the rms deviation between $E(t)$ in HYCOM with resolutions of $\Delta x = 100m, 50m, 20m$ is minimized for $7000\,s < t < 10000\,s$. This calibration results in the optimized coefficient values of $K_{max} = 2500\,cm^2 s^{-1}$ for KPP and $C_A = 0.15$ for TP. Using these parameters, snapshots of the gravity current at the different times, and from different horizontal resolutions, show good agreement between the results obtained with KPP and TP (Figs. 11,12 and also Fig. 11b, 11e, 12b, 12e vs Fig. 5).

Fig. 13 shows the distribution of shear Richardson numbers along the flow direction averaged over the spanwise direction for both the KPP and TP experiments at selected horizontal resolution of $\Delta x = 100\,m$ and at instant $t = 13050\,s$. The comparison is performed for layers 3 and 4 (out of 5) because $Ri$ is not defined at the top and the bottom layers in TP. Furthermore, the entrainment into layer 2 is weak. In KPP, $Ri$ is defined at the layer interfaces, whereas it is defined at the middle of the layers in TP. In order to remove this difference, a linear interpolation was used to estimate $Ri$ in the middle of the layers in KPP. As shown in Fig. 13, $Ri$ is mostly in the range of 0.1 to 0.2, which is quite small compared to $Ri_c$. This finding explains why the overall results are insensitive to the value of $Ri_c$.

### 5.4. Further examinations:

In order to explore the sensitivity of our results to mixing induced by the bottom shear stress, we explored the impact of the BBL formulation given in eq. (3) by running all KPP experiments (5 different resolutions and 2 different $K_{max}$) with and without BBL. No difference has been found. Mixing takes place from above the gravity current, in agreement with the picture put forth by Peters et al. (2004a) based on observations of the Red Sea overflow in a narrow channel, in which the bottom properties are largely preserved, and mixing is mostly confined to the shear layer above a thick and homogeneous bottom layer. The BBL formulation thus does not play a role in the present set of numerical experiments, but it might become more important in overflows subject to lateral spreading.

We have noted above that the laboratory experiments of Ellison and Turner (1959) had rather large slope angles, much larger than in nature. This raised the question how well the

TP scheme handles different slope angles. In order to examine this issue, several additional experiments have been conducted with slope angles of $\theta = 2°$ and $\theta = 1°$ using modified KPP and TP formulations at a selected horizontal resolution of $\Delta x = 100\,m$. The results indicate that entrainment curves $E(t)$ from KPP remain virtually unchanged in response to changes in the slope angle (Fig. 14a), while those from TP exhibit stronger variations. In response to a 3.5-fold decrease of the slope angle, the equilibrium entrainment parameter decreases by about 20% in TP (Fig. 14b).

## 6. Summary and discussion

Our understanding of the dynamics of overflows is based on the results of dedicated observational programs in the Mediterranean Sea overflow (Baringer and Price, 1997a,b), Denmark Strait overflow (Girton et al., 2001; 2003), Red Sea overflow (Peters et al., 2004a,b), Faroe Bank Channel (Price, 2004) and Antarctic Ocean (Gordon et al., 2004), and also of laboratory tank experiments (e.g., Ellison and Turner, 1959; Simpson, 1987; Hallworth et al., 1996; Monaghan et al., 1999; Baines, 2001; Cenedese and Whitehead, 2004), and process modeling studies (e.g., Özgökmen and Chassignet, 2002; Özgökmen et al., 2003; Özgökmen et al., 2004a,b). It is important that this knowledge is incorporated in OGCMs in the form of appropriate mixing parameterizations.

In this study, experiments are conducted using an OGCM, HYCOM, in an idealized setting that represents the basics of shear-induced mixing in bottom gravity currents, that is, the flow of a dense water mass released at the top of a wedge, which is 20 km long, 2 km wide, and has a slope of $\theta = 3.5°$ with respect to the horizontal. Similar experiments have been carried out by Özgökmen et al. (2004a) using a high-order nonhydrostatic spectral element model, Nek5000, a general Navier-Stokes solver developed by Fischer (1997). Our HYCOM experiments are configured as similar as possible to the Nek500 setting, and are conducted with 5 different horizontal resolutions of 1000m, 500m, 100m, 50m, and 20m. In HYCOM, two mixing parameterizations are used, (i) KPP (Large et al., 1994, 1999), a class of multi-purpose mixing algorithms which includes a shear-induced mixing scheme based on results from Pacanowski and Philander (1981), and (ii) TP, which has been developed for overflows by Hallberg (2000) based on laboratory results from Ellison and Turner (1959) and

Turner (1986). Both schemes are based on the local gradient Richardson number, but they differ in that a vertical diffusivity is used in KPP while the entrainment velocity is specified in TP. We explore how results from HYCOM with KPP and TP compare to each other and to those from Nek5000, and whether results change significantly as a function of the model resolution.

It is found that KPP results in significantly less gravity current entrainment than that in the reference experiment with Nek5000, while TP leads to significantly more entrainment than both. Specifically, the entrainment parameter (defined in section 5.2) converges to $E \approx 1 \times 10^{-3}$ in experiments with KPP, $E \approx 8 \times 10^{-3}$ in experiments with TP, whereas $E \approx 4 \times 10^{-3}$ in the 3D experiment with Nek5000. The results are fairly independent of the horizontal grid resolution. KPP and TP are then tuned using results from Nek5000, and it is found that this requires an increase of $K_{max}$ from $50\, cm^2 s^{-1}$ to $2500\, cm^2 s^{-1}$ for KPP, and a decrease of $C_A$ from 1 to 0.15 for TP.

Given that the parameters of KPP and TP needed to be changed significantly in order for them to match the results from high-resolution nonhydrostatic 3D model runs, further discussion of the structure of these parameterization schemes is needed. With respect to the original experiments analyzed by Ellison and Turner (1959) and Turner (1986), which underlie TP, one could raise questions concerning viscous effects of bottom and side boundaries in a very small tank 2 m long and 10 cm wide, and a flow only 10 cm deep. Other questions concern the large slopes in the tank experiments, $12° \leq \theta \leq 90°$, compared to small angles, $\theta < 5°$ in nature. However, the fundamental reason why the parameter values of Hallberg's (2000) TP scheme have to be considered adjustable is that they were taken unchanged from an algorithm employing the bulk Richardson number of a single-layer bottom gravity flow and and applied in a new algorithm employing gradient Richardson numbers in a multi-layered shear flow. The differences between these two physical settings are vast.

Numerical experiments by Papadakis et al. (2003) provide further incentive to tune TP. They conducted simulations of the Mediterranean Sea outflow using HYCOM with TP with encouraging results. However, in order to obtain a realistic path of the overflow and to achieve the generation of subsurface eddies (Meddies), in a somewhat ad-hoc approach they resorted to applying the TP scheme only every 144-th time step rather than at every step.

Further, when TP is used as a general shear-induced mixing parameterization in North Atlantic simulations of HYCOM, it leads to unrealistically high mixing rates in the equatorial regions.

Problems with KPP have also become obvious. The KPP-modeled Mediterranean outflow sinks far deeper than observations in recent high-resolution (1/12°) simulations using HYCOM, indicating that mixing induced by KPP is insufficient when directly applied to overflows. We have already noted that KPP cannot be universally valid because of its simplistic structure, a dimensional constant times a function of a nondimensional parameter, $Ri$. Specifically, $K_{max}$ was determined from LES modeling of the diurnal cycle of surface mixed layer at the equator subject to a specific forcing. Physical intutition leads to the expectation that $K_{max}$ should vary with the strength of the forcing and that it should not be expected that this particular value of $K_{max}$ to hold in bottom gravity current mixing.

Noting that the original development of KPP (Large and Gent, 1999) in addition to LES simulations also contemplated the oceanic turbulence observations of Peters et al. (1988), we reviewed their measurements in the light of our current study. Within the high-shear, low-$Ri$ setting of the Pacific Equatorial Undercurrent at 140$^o$W, the 1984 Tropic Heat 1 Experiment found much stronger mixing at night, when the ocean loses heat and the surface mixed layer undergoes convection, than during daytime, when the solar heat input stabilizes the upper ocean. Hence, in this environment the forcing of the turbulence has a nighttime maximum. Fig. 15 depicts hourly averages of the eddy diffusivity of heat, $K_h$, as function of the local $Ri$ separately for daytime and nighttime. While the overall shape of the average curve $K_h = K_h(Ri)$ does not change significantly between day and night, nighttime adds large $K_h$ to the high-$K_h$ end of the curve. This is like varying $K_{max}$ in KPP. Therefore, turbulence parameterizations should include both a dependence on the forcing and a dependence on the flow Richardson number. This requirement holds for TP but not for KPP.

The preceding requirement is consistent with common and accepted turbulence parameterizations more complex than KPP and TP. Two-equation turbulence closures of all varieties (e.g., Mellor and Yamada, 1982; Baumert and Peters, 2004) represent the $Ri$-dependence as "stability functions," while the dependence on the forcing is handled by the pair of predictive differential equations for the turbulent kinetic energy and another variable related to the turbulent length scale. Sub-grid scale schemes commonly employed in LES models are similar, if simpler. Following, e.g., Smagorinsky (1963), Deardorff (1973), Schumann (1991), and Stevens (2000), one can write

$$K = c\, l^2\, |S|\, f(Ri)\ , \tag{14}$$

where $S^2 = \frac{\partial u_i}{\partial x_j} D_{ij}$ $(i, j = 1, 2, 3)$ is the resolved strain rate. Further, $D_{ij} = \partial u_i/\partial x_j + \partial u_j/\partial x_i$ denotes the resolved scale deformation using a grid spacing proportional to $l$ (typically, $l = (\Delta x \Delta y \Delta z)^{1/3}$), and $c$ is an empirical constant. The effect of stratification is incorporated by specifying a monotonously decreasing function that satisfies

$$f(Ri) \ = \ \begin{cases} 1 \ \text{ for } \ Ri = 0 \\ 0 \ \text{ for } \ Ri \geq Ri_c \end{cases} \ . \tag{15}$$

The detailed shape of this curve would require additional information about the mixing process (e.g. as in the Peters et al. (1988) observations), but even a linear relationship could suffice as a first-order approximation.

The key point is that the dynamical factor determining the amplitude of the mixing coefficient at low $Ri$, which is a function of the resolved strain rate, $l^2\,|S|$, is replaced by a peak diffusivity of $K|_{Ri=0} = K_{max} = 50\, cm^2 s^{-1}$ in KPP, based on results from a physical regime quite different than oceanic overflows. In contrast, by relating $w_E$ to $\Delta U$, TP does avoid a hard limit for peak effective diffusivity, and the implied diffusivity includes both a dependence on the flow Richardson number and on the forcing via the resolved model local velocity structure $\Delta U$. This explains why the extrainment parameter in TP changes in response to variations in the slope angle whereas KPP does not seem to show any response.

In future studies, it will be explored how KPP, a popular mixing model for many OGCMs, can be modified to incorporate the dependence of mixing coefficients on the forcing for overflow scenarios. Also, it needs to be further investigated how accurately TP captures the dependence of the entrainment on the slope angle.

Finally, the environment used in this study – as well as in the experiments of Ellison and Turner (1959) – is homogeneous, whereas ambient stratification can have a significant effect on the nature of the mixing process and entrainment (e.g., Baines, 2001), and therefore the dynamics of overflows. In order for mixing parameterizations to be applicable to the ocean, the effect of ambient stratification needs to be taken into account. This issue will also be explored in the near future.

**Acknowledgments**

We greatly appreciate the support of National Science Foundation via grants OCE 0336799 and DMS 0209326, the Office of Naval Research grant N00014-03-1-0425 and the Mathematical, Information, and Computational Sciences Division subprogram of the Office of Advanced Scientific Computing Research, U.S. Department of Energy, under Contract W-31-109-ENG-38. The authors benefited greatly from discussions with the other PIs of the Climate Process Team on gravity current entrainment, G. Danabasoglu, T. Ezer, A. Gordon, S. Griffies, P. Gent, R. Hallberg, W. Large, S. Legg, J. Price, P. Schopf and J. Yang. We also thank two anonymous reviewers for their constructive comments, which helped greatly improve the manuscript.

## References

Baines, P. G., 2001: Mixing in flows down gentle slopes into stratified environments. *J. Fluid Mech.*, **443**, 237–270.

Baringer, M. O., and J. F. Price, 1997a: Mixing and spreading of the Mediterranean outflow. *J. Phys. Oceanogr.*, **27**, 1654–1677.

Baringer, M. O., and J. F. Price, 1997b: Momentum and energy balance of the Mediterranean outflow. *J. Phys. Oceanogr.*, **27**, 1678–1692.

Baumert, H. and H. Peters, 2004: Turbulence closure, steady state, and collapse into waves. *J. Phys. Oceanogr.*, **34**, 505-512.

Beckmann, A., and R. Döscher, 1997: A method for improved representation of dense water spreading over topography in geopotential-coordinate models. *J. Phys. Oceanogr.*, **27**, 581–591.

Bleck, R., 2002: An oceanic general circulation model framed in hybrid isopycnic-Cartesian coordinates. *Ocean Modelling*, **4**, 55-88.

Bower, A. S., H. D. Hunt, and J. F. Price, 2000: Character and dynamics of the Red Sea and Persian Gulf outflows. *J. Geophys. Res.*, **105**, 6387–6414.

Britter, R. E., and P. F. Linden, 1980: The motion of the front of a gravity current traveling down an incline. *J. Fluid Mech.*, **99**, 531–543.

Cenedese, C., J.A. Whitehead, T.A. Ascarelli, and M. Ohiwa, 2004: A dense current flowing down a sloping bottom in a rotating fluid. *J. Phys. Oceanogr.*, **34**, 188-203.

Chassignet, E.P., L.T. Smith, G.R. Halliwell, and R. Bleck, 2003: North Atlantic simulation with the HYbrid Coordinate Ocean Model (HYCOM): Impact of the vertical coordinate choice, reference density, and thermobaricity. *J. Phys. Oceanogr.*, **33**, 2504-2526.

Corcos, G. M., and F. S. Sherman, 1984: The mixing layer: deterministic models of a turbulent flow. Part 1. Introduction and the two-dimensional flow. *J. Fluid Mech.*, **139**, 29–65.

Deardorff, J.W., 1973: A numerical study of three-dimensional turbulent channel flow at large Reynolds numbers. *J. Fluid Mech.*, **41**, 453-480.

Ellison, T. H., and J. S. Turner, 1959: Turbulent entrainment in stratified flows. *J. Fluid Mech.*, **6**, 423–448.

Ezer, T. and G.L. Mellor, 2004: A generalized coordinate ocean model and comparison of the bottom boundary layer dynamics in terrain-following and in z-level grids. *Ocean Modelling*, **6**, 379-403.

Fernando, H.J.S., 2000: Aspects of stratified turbulence. In *Developments in Geophysical Turbulence*, eds: R.M. Kerr and Y. Kimura, pp. 81-92, Kluwer.

Fischer, P. F., and J. S. Mullen, 2001: Filter-Based Stabilization of Spectral Element Methods. *Comptes rendus de l'Académie des sciences Paris, t. 332, -Série I - Analyse numérique*, 265–270.

Fischer, P. F., 1997: An overlapping Schwarz method for spectral element solution of the incompressible Navier-Stokes equations. *J. of Comp. Phys.* **133**, 84–101.

Fischer, P. F., N. I. Miller, and H. M. Tufo, 2000: An overlapping Schwarz method for spectral element simulation of three-dimensional incompressible flows. In *Parallel Solution of Partial Differential Equations*. Springer-Verlag, ed. by P. Björstad and M. Luskin, 159–181.

Flierl, G. R., M. E. Stern, and J. A. Whitehead, 1981: The physical significance of modons: laboratory experiments and general integral constraints. *Dyn. Atmos. Oceans*, **7**, 233–263.

Gallacher, P. and S. Piacsek, 2004: Comparisons of nonhydrostatic, quasi-hydrostatic and hydrostatic simulations of internal bores. *Continental Shelf Res.*, in press.

Gargett, A. E., 1984: Vertical diffusivity in the ocean ineterior. *J. Mar. Res.*, **42**, 359–393.

Girton, J. B., and T. B. Sanford, 2003: Descent and modification of the overflow plume in the Denmark Strait. *J. Phys. Oceanogr.*, **33**, 1351-1363.

Girton, J. B., T. B. Sanford, and R. H. Käse, 2001: Synoptic sections of the Denmark Strait overflow. *Geophys. Res. Lett.*, **28**, 1619–1622.

Gordon, A., E. Zambianchi, A. Orsi, M. Visbeck, C. Giulivi, T. Whitworth III and G. Spezie, 2004: Energetic plumes over the western Ross Sea continental slope. *Geophys. Res. Lett.*, in press.

Gregg, M.C., H. Peters, J.C. Wesson, N.S. Oakey, and T.S. Shay, 1985: Intensive measurements of turbulence and shear in the equatorial undercurrent. *Nature*, **6042**, 140-144.

Griffies, S.M., R.C. Pacanowski, R.W. Hallberg, 2000: Spurious diapycnal mixing associated with advection in a z-coordinate ocean model. *Mon. Weather Rev.*, **128**, 538-564.

Griffiths, R. W., 1986: Gravity currents in rotating systems. *Annu. Rev. Fluid Mech.*, **18**, 59–89.

Hallberg, R., 2000: Time integration of diapycnal diffusion and Richardson number dependent mixing in isopycnal coordinate ocean models. *Mon. Wea. Rev.*, **128**(5), 1402–1419.

Halliwell, G.R., 2004: Evaluation of vertical coordinate and vertical mixing algorithms in the HYbrid-Coordinate Ocean Model (HYCOM). *Ocean Modell.*, **7**, 285-322.

Hallworth, M. A., H. E. Huppert, J. C. Phillips, and S. J. Spark, 1996: Entrainment into two-dimensional and axisymmetric turbulent gravity current. *J. Fluid Mech.*, **308**, 289–311.

Härtel, C., E. Meiburg, and F. Necker, 2000: Analisys and direct numerical simulation of the flow at a gravity-current head, Part 1: Flow topology and front speed for slip and no-slip boundaries. *J. Fluid Mech.*, **418**, 189–212.

Jacobsen, J. P., 1913: Beitrag zur Hydrographie der dänischen Gewässer. *Medd. Komm. Havundersøg. Kbh. (Hydro)*, **2**, 99 pp.

Johnson, G. C., T. B. Sanford and M. O'Neil Baringer, 1994a: Stress on the Mediterranean Outflow Plume: Part I. Velocity and Water Property Measurements. *J. Phys. Oceanogr.*, **24**, 2072–2083.

Johnson, G. C., R.G. Lueck, and T. B. Sanford, 1994b: Stress on the Mediterranean Outflow Plume: Part II. Turbulent dissipation and shear measurements. *J. Phys. Oceanogr.*, **24**, 2084–2092.

Jungclaus, J. H., and G. Mellor, 2000: A three-dimensional model study of the Mediterranean outflow. *J. Mar. Sys.*, **24**, 41–66.

Keulegan, G. H., 1958: The motion of saline fronts in still water. *U.S. Nat. Bur. Stand.*, Report no. 5831.

Killworth, P. D., and N. R. Edwards, 1999: A turbulent bottom boundary layer code for use in numerical ocean models. *J. Phys. Oceanogr.*, **29**, 1221–1238.

Killworth, P. D., 1977: Mixing on the Weddell Sea continental slope. *Deep-Sea Res.*, **24**, 427–448.

Klaassen, G. P., and W. R. Peltier, 1991: The influence of stratification on secondary instability in free shear layers. *J. Fluid Mech.*, **227**, 71–106.

Large, W.G., 1998: Modeling and parameterizing ocean planetary boundary layer. In *Ocean Modelling and Parameterization*, eds: E.P. Chassignet and J. Verron, Kluwer, pp. 45-80.

Large, W.G., and P. R. Gent, 1999: Validation of vertical mixing in an equatorial ocean model using large eddy simulations and observations. *J. Phys. Oceanogr.*, **29**, 449-464.

Large, W. G., J.C. McWilliams, and S.C. Doney, 1994: Oceanic vertical mixing: A review and a model with a nonlocal boundary layer parameterization. *Rev. Geophys.*, **32**, 363-403.

Matt, S., 2004: Transport and entrainment in the Red Sea outflow. M.S. Thesis, University of Miami, 93 pp.

Mellor, G. L., and T. Yamada, 1982: Development of a turbulence closure model for geophysical fluid problems, *Rev. Geophys. Space Phys.*, **20**,851–875.

Monaghan, J. J., R. A. F. Cas, A. M. Kos, and M. Hallworth, 1999: Gravity currents descending a ramp in a stratified tank. *J. Fluid Mech.*, **379**, 39–70.

Murray, S. P., and W. E. Johns, 1997: Direct observations of seasonal exchange through the Bab el Mandab Strait. *Geophys. Res. Lett.*, **24**(21), 2557–2560.

Nakano, H., and N. Suginohara, 2002: Effects of bottom boundary layer parameterization on reproducing deep and bottom waters in a world ocean model. *J. Phys. Oceanogr.*, **32**, 1209–1227.

Nielsen, A. H., and J. J. Rasmussen, 1996: Formation and temporal evolution of the Lamb-dipole. *Phys. Fluids*, **9**, 982–991.

Özgökmen T.M., P.F. Fischer, J. Duan and T. Iliescu, 2004a: Three-dimensional turbulent bottom density currents from a high-order nonhydrostatic spectral element model. *J. Phys. Oceanogr.*, **34**/9, 2006-2026.

Özgökmen T.M., P.F. Fischer, J. Duan and T. Iliescu, 2004b: Entrainment in bottom gravity currents over complex topography from three-dimensional nonhydrostatic simulations. *Geophys. Res. Lett.*, **31**, L13212, doi:10.1029/2004GL020186.

Özgökmen, T. M., W. Johns, H. Peters, and S. Matt, 2003: Turbulent mixing in the Red Sea outflow plume from a high-resolution nonhydrostatic model. *J. Phys. Oceanogr.*, **33/8**, 1846–1869.

Özgökmen, T. M., and E. Chassignet, 2002: Dynamics of two-dimensional turbulent bottom gravity currents. *J. Phys. Oceanogr.*, **32**, 1460–1478.

Pacanowski, R.C., and S.G.H. Philander, 1981: Parameterization of vertical mixing in numerical models of the tropical oceans. *J. Phys. Oceanogr.*, **11**, 1443-1451.

Papadakis, M. P., E. P. Chassignet, and R. W. Hallberg, 2003: Numerical simulations of the Mediterranean Sea outflow: Impact of the entrainment parameterization in an isopycnic coordinate ocean model. *Ocean Modelling*, **5**, 325–356.

Peters, H., W.E. Johns, A.S. Bower, and D.M. Fratantoni, 2004a: Mixing and entrainment in the Red Sea outflow plume. I. plume structure. *J. Phys. Oceanogr.*, in press.

Peters, H., and W.E. Johns, 2004b: Mixing and entrainment in the Red Sea outflow plume. II. turbulence characteristics. *J. Phys. Oceanogr.*, in press.

Peters, H., and M.C. Gregg, 1988: In the parameterization of equatorial turbulence. *J. Geophys. Res.*, **93**, 1199-1218.

Price, J.F., 2004: A process study of the Faroe Bank Channel overflow. *Geophys. Res. Abstracts*, **6**, 07788.

Price, J., and J. Yang, 1998: Marginal sea overflows for climate simulations. In *Ocean Modelling and Parameterization*, ed. by E. P. Chassignet and J. Verron, pp. 155–170.

Price, J. F., and M. O. Baringer, 1994: Outflows and deep water production by marginal seas. *Prog. Oceanogr.*, **33**, 161–200.

Price, J. F., M. O. Baringer, R. G. Lueck, G. C. Johnson, I. Ambar, G. Parrilla, A. Cantos, M. A. Kennelly, and T. B. Sanford, 1993: Mediterranean outflow mixing and dynamics. *Science*, **259**, 1277–1282.

Schumann, U., 1991: Subgrid length-scales for large-eddy simulations of stratified turbulence. *Theoret. Comput. Fluid Dynamics*, **2**, 279-290.

Simpson, J. E., 1987: *Gravity Currents in the Environment and the Laboratory.* John Wiley and Sons, New York, 244 pp.

Simpson, J. E., 1982: Gravity currents in the laboratory, atmosphere, and the ocean. *Ann. Rev. Fluid Mech.*, **14**, 213–234.

Simpson, J. E., 1972: Effects of the lower boundary on the head of a gravity current. *J. Fluid Mech.*, **53**, 759–768.

Simpson, J. E., 1969: A comparison between laboratory and atmospheric density currents. *Quart. J. Roy. Met. Soc.*, **95**, 758–765.

Smagorinksy, J., 1963: General circulation experiments with the primitive equations. I. the basic experiment. *Mon. Weath. Rev.*, **91**, 99-164.

Smith, R. A., 1991: Maximization of vortex entropy as an organizing principle in intermittent, decaying, two-dimensional turbulence. *Phys. Rev.*, **A 43**, 1126–1129.

Smith, P. C., 1975: A streamtube model for bottom boundary currents in the ocean. *Deep-Sea Res.*, **22**, 853–873.

Stevens, B., C.-H. Moeng, and P.P. Sullivan, 2000: Entrainment and subgrid lengthscales in large-eddy simulations of atmospheric boundary-layer flows. In *Developments in Geophysical Turbulence*, eds: R.M. Kerr and Y. Kimura, pp. 253-270, Kluver.

Tufo, H. M., and P. F. Fischer, 1999: Terascale Spectral Element Algorithms and Implementations. Gordon Bell Prize submission, *Proc. of the ACM/IEEE SC99 Conf. on High Performance Networking and Computing*. IEEE Computer Soc., CDROM.

Turner, J. S., 1986: Turbulent entrainment: The development of the entrainment assumption, and its applications to geophysical flows. *J. Fluid Mech.*, **173**, 431–471.

Willebrand, J., B. Barnier, C. Böning, C. Dieterich, P. Harrmann, P. D. Killworth, C. LeProvost, Y. Jia, J.-M. Molines, and A. L. New, 2001: Circulation characteristics in three eddy-permitting models of the North Atlantic. *Prog. Oceanogr.*, **48**, 123–161.

Winton, M., R. Hallberg, and A. Gnanadesikan, 1998: Simulation of density-driven frictional downslope flow in z-coordinate ocean models. *J. Phys. Oceanogr.*, **28**, 2163–2174.

Table 1: Parameters of the Nek5000 nonhydrostatic model simulation.

| | |
|---|---|
| Domain Size $(L_x, L_z = H, L_y)$ | $(10^4\,\mathrm{m}\,, 10^3\,\mathrm{m}\,, 2\times 10^3\,\mathrm{m})$ |
| Slope angle | $\theta = 3.5°$ |
| Rayleigh number | $Ra = 5\times 10^6$ |
| Prandtl number | $Pr = 1$ |
| Diffusivity ratio | $r = 2\times 10^{-2}$ |
| Salinity range | $\Delta S = 1.0\,\mathrm{psu}$ |
| Number of elements $(x, z, y)$ | $50\,, 8\,, 10$ |
| Polynomial degree | $N = 10$ |
| Number of grid points | $4\times 10^6$ |
| Time step | $\Delta t = 0.85\,\mathrm{s}$ |

Table 2: Parameters of the HYCOM simulations.

| | KPP | TP |
|---|---|---|
| Domain Size $(L_x, L_z = H, L_y)$ | $(3\times 10^4\,\mathrm{m}\,, 1.6\times 10^3\,\mathrm{m}\,, 2\times 10^3\,\mathrm{m})$ | same |
| Slope angle | $\theta = 3.5°$ | same |
| Mixing parameters | $K_{max} = 50,\;\; 2500\,cm^2 s^{-1}$ | $C_A = 1,\ 0.15$ |
| Salinity range | $\Delta S = 1.0\,\mathrm{psu}$ | same |
| Horizontal resolution | $\Delta x = \Delta y = 20\,, 50\,, 100\,, 500\,, 1000\,\mathrm{m}$ | same |
| Vertical resolution | 5, 11 layers | same |
| Time step | $\Delta t = 1\,, 9\,\mathrm{s}$ | same |

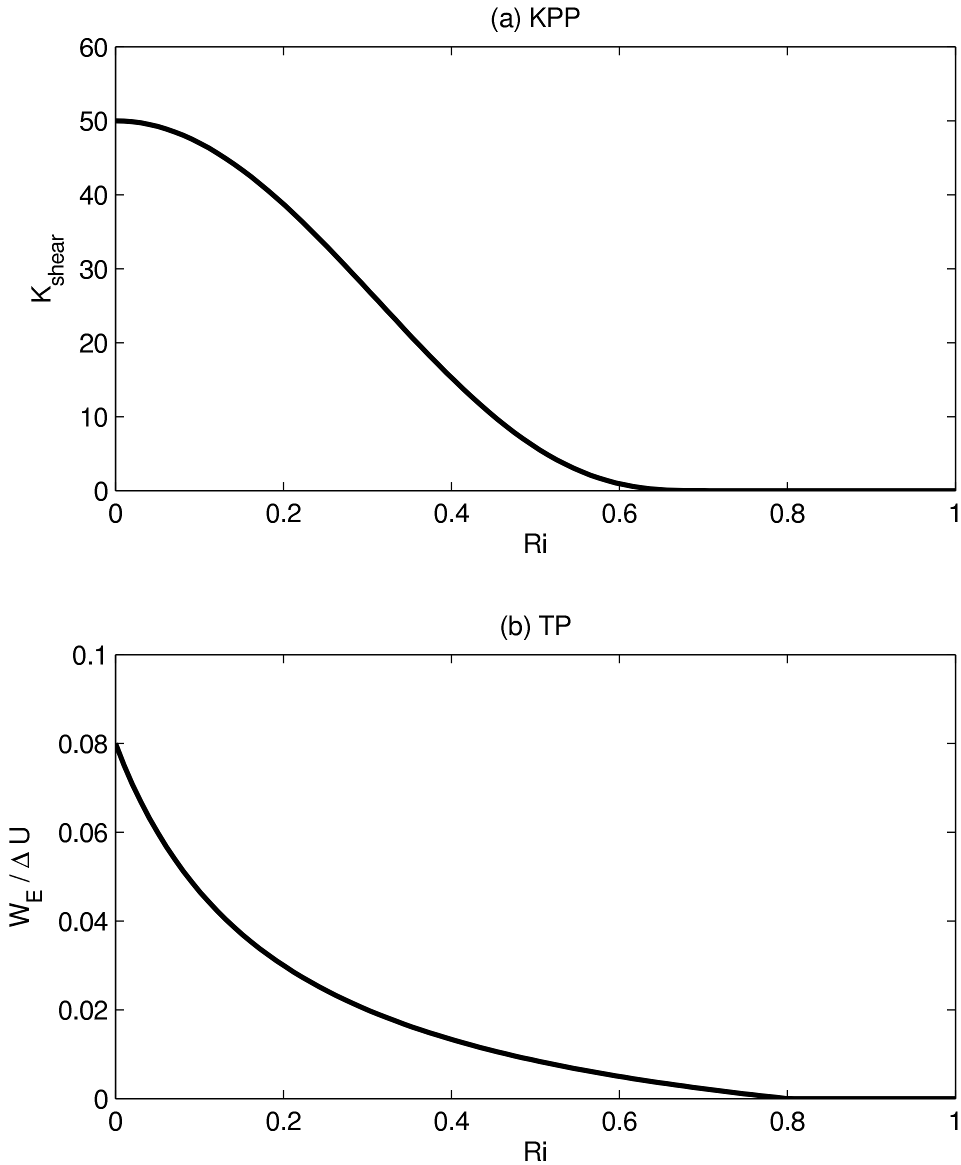


Figure 1: Mixing curves of KPP and TP. (a) $K_{shear}\,(cm^2\,s^{-1})$ as a function of $Ri$ in KPP, and (b) $w_E/\Delta U$ as a function of $Ri$ in TP.

(a)

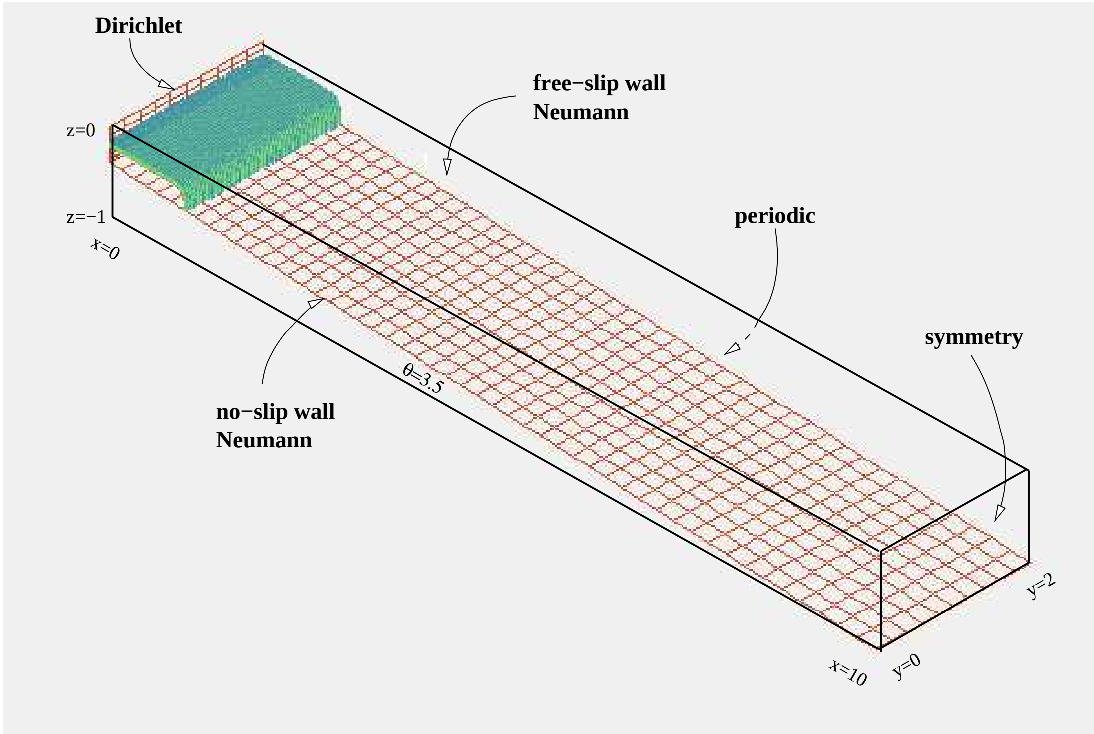


(b)

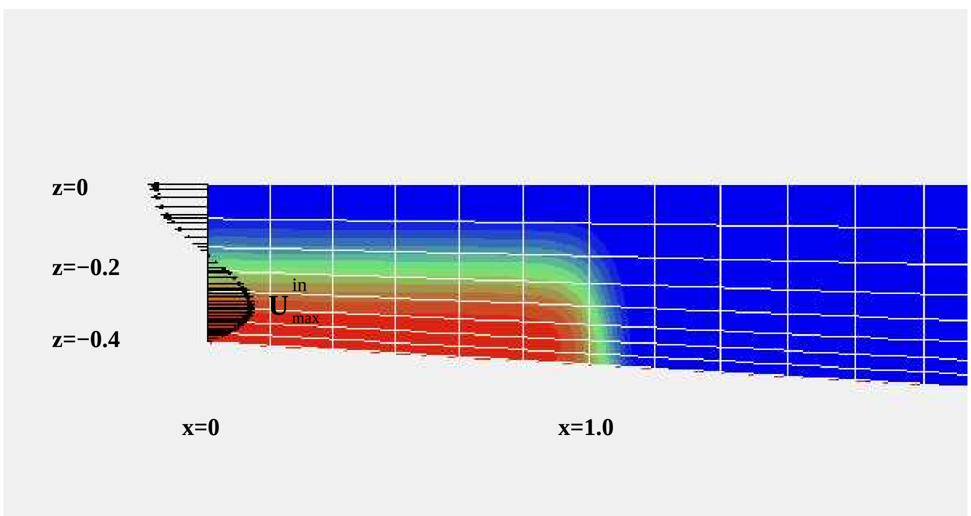


Figure 2: Configuration of experiments in Nek5000. (a) Schematic depiction of the domain geometry and boundary conditions (length scale is in km). (b) Velocity profile at the forcing boundary and the initial distribution of salinity. Distribution of elements is depicted in the background.

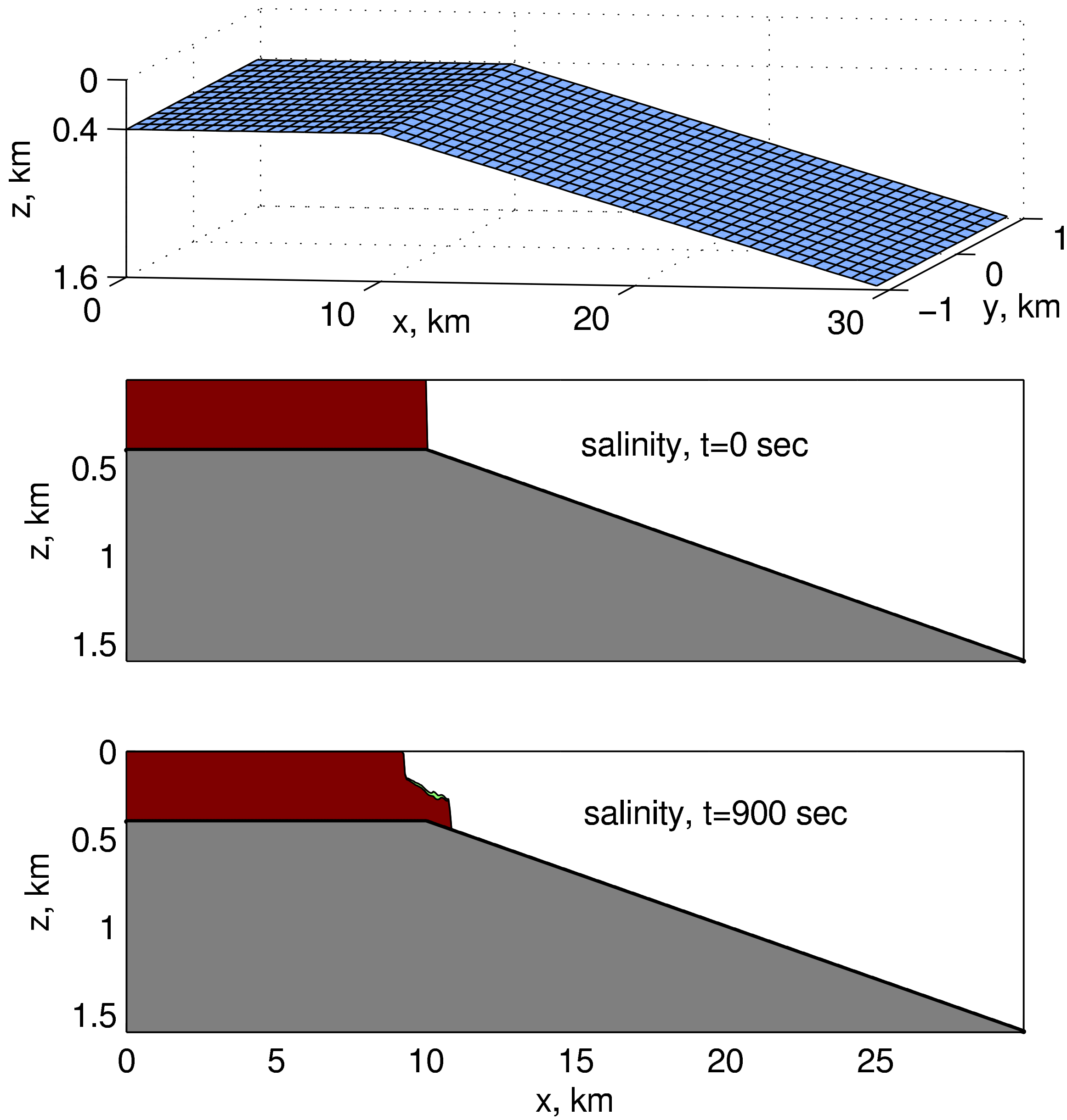


Figure 3: Computational domain and initial conditions in HYCOM experiments. (a) Domain geometry in 3D, (b) the initial salinity distribution ($x-z$ plane), and (c) salinity distribution at $t = 15$ min.

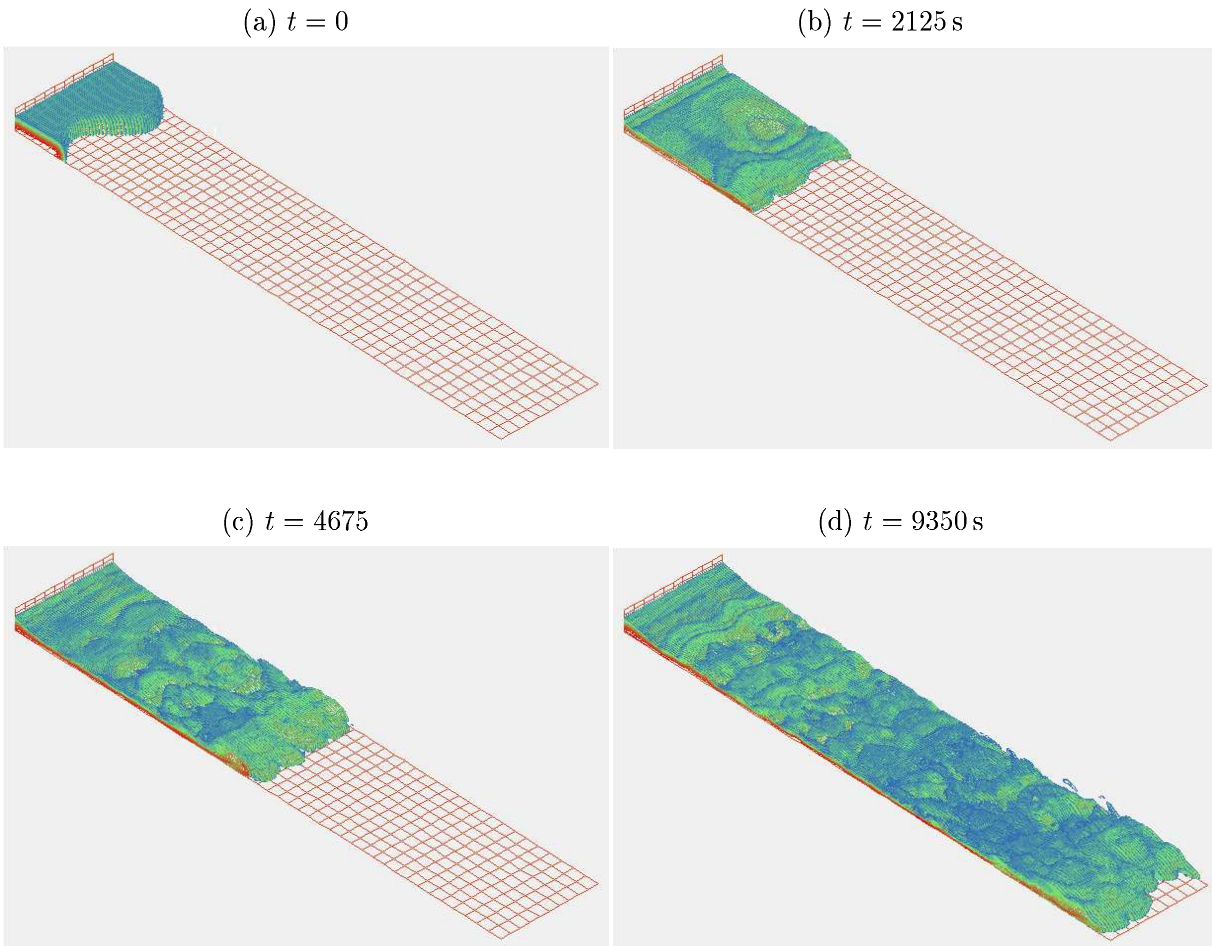


Figure 4: Distribution of salinity surface $0.3 \leq S \leq 0.6$ in Nek5000 at (a) $t = 0$, (b) $t = 2125\,\mathrm{s}$ ($\approx 0.6\,\mathrm{h}$), (c) $t = 4675\,\mathrm{s}$ ($\approx 1.3\,\mathrm{h}$), (d) $t = 9350\,\mathrm{s}$ ($\approx 2.6\,\mathrm{h}$).

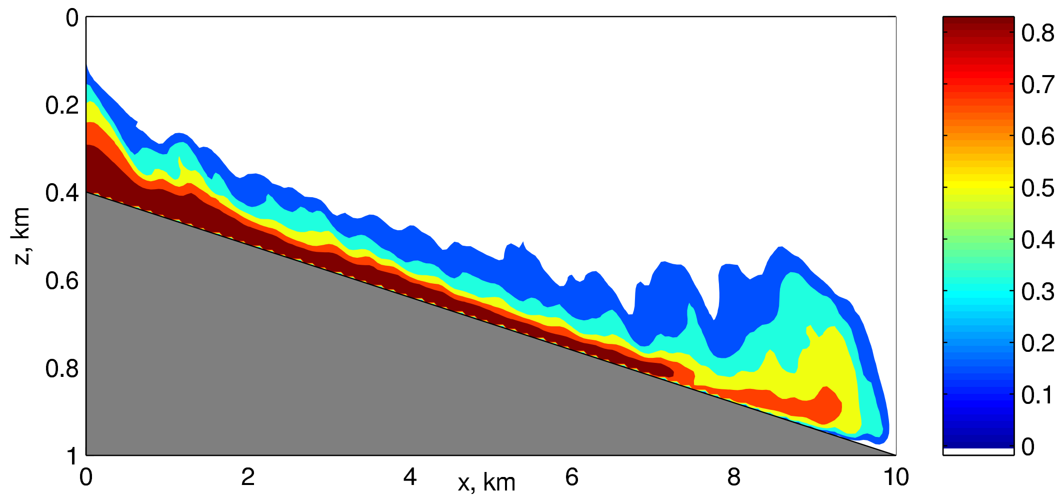


Figure 5: Distribution of span-wise averaged salinity in Nek5000 at $t = 9350\,\mathrm{s}$.

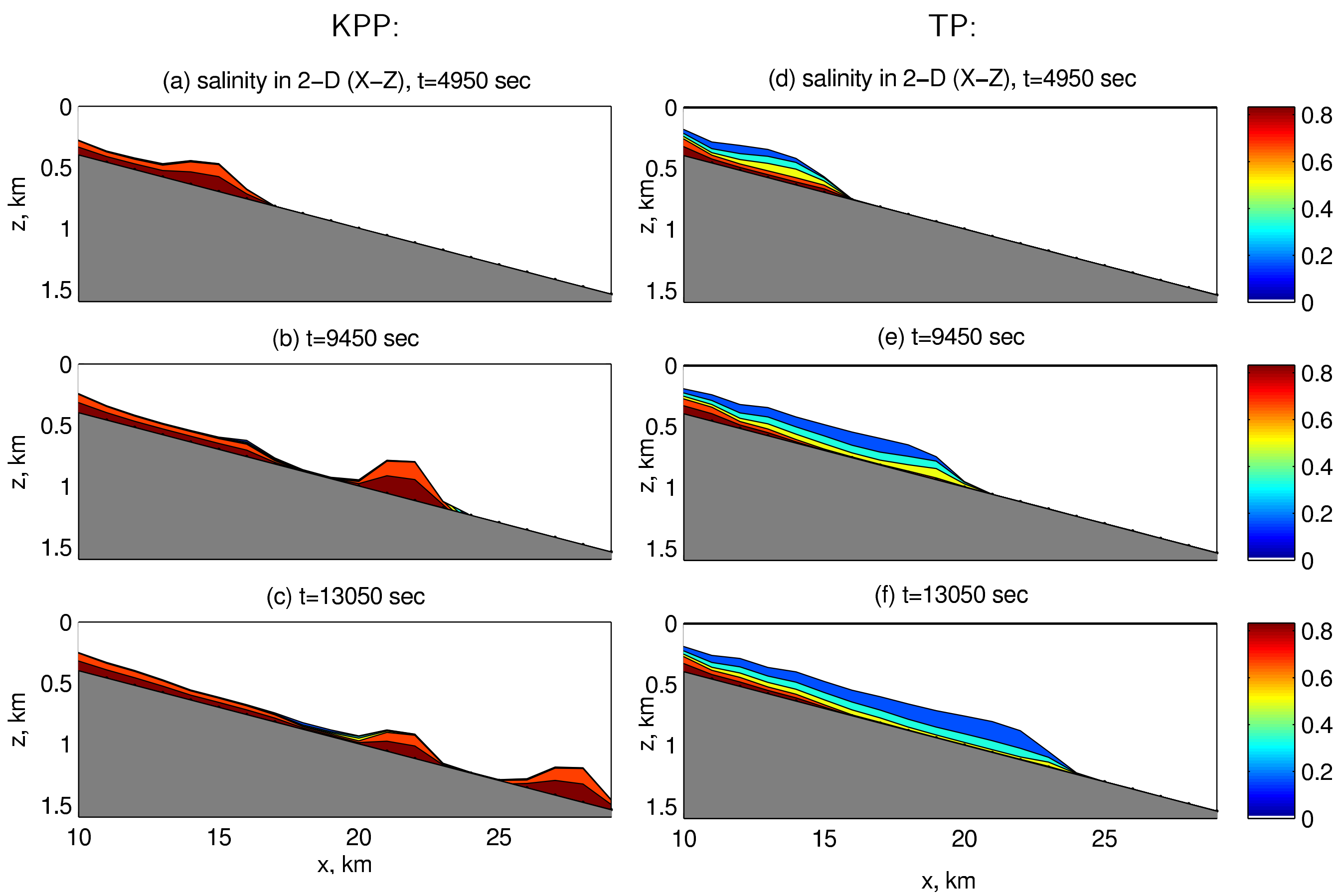


Figure 6: Evolution of the distribution of salinity perturbation ($S' = S - S_0$) in time in HYCOM experiments (a) $t = 4960\,\mathrm{s}$, (b) $t = 9450\,\mathrm{s}$, and (c) $t = 13050\,\mathrm{s}$ using KPP with $\Delta x = 1000$ m, and (d), (e), (f) using TP.

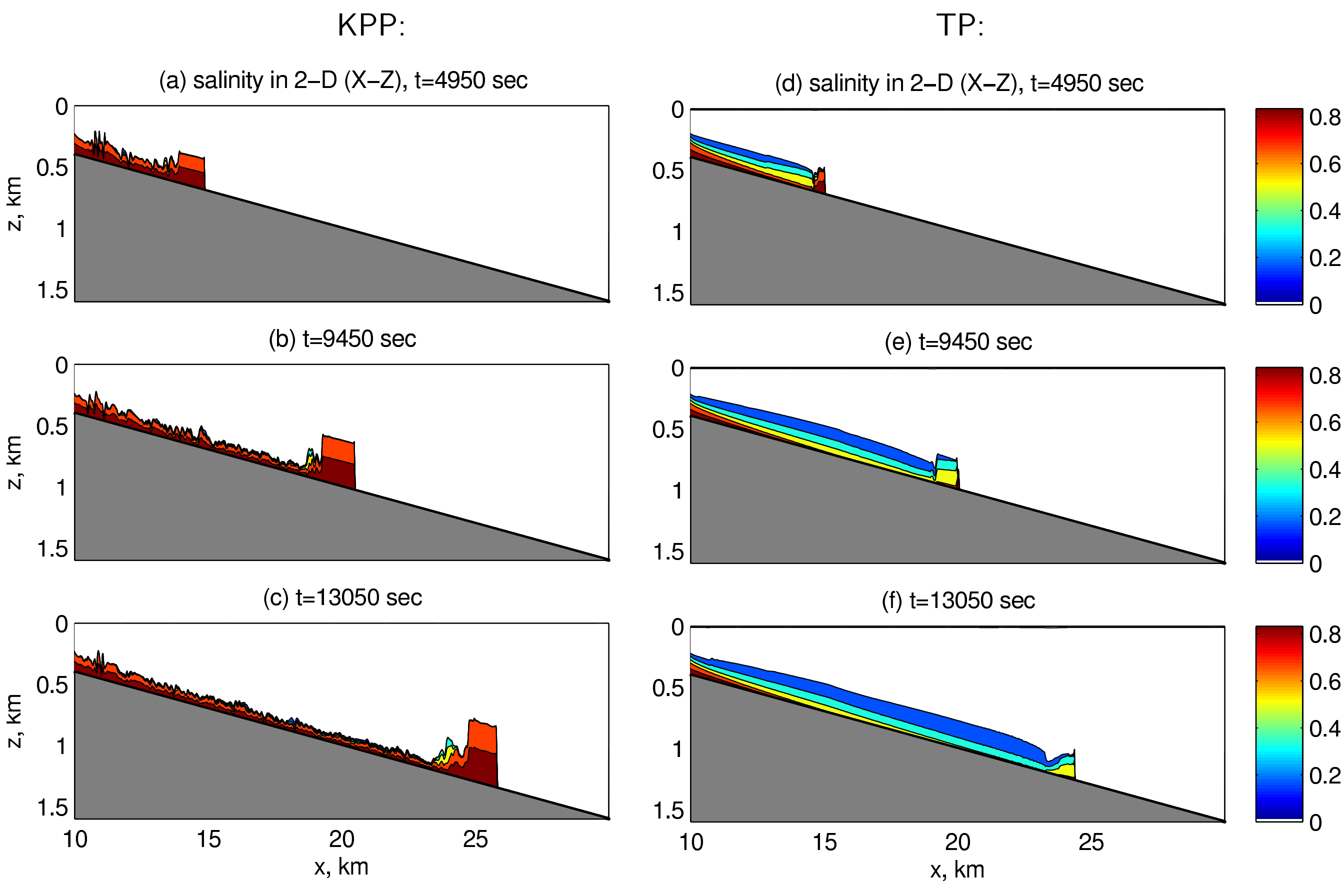


Figure 7 : Evolution of salinity distribution in time in HYCOM experiments (a) spanwise-average at $t = 4960\,\mathrm{s}$, (b) spanwise-average at $t = 9450\,\mathrm{s}$, and (c) spanwise-average at $t = 13050\,\mathrm{s}$ using KPP with $\Delta x = 20$ m, and (d), (e), (f) using TP.

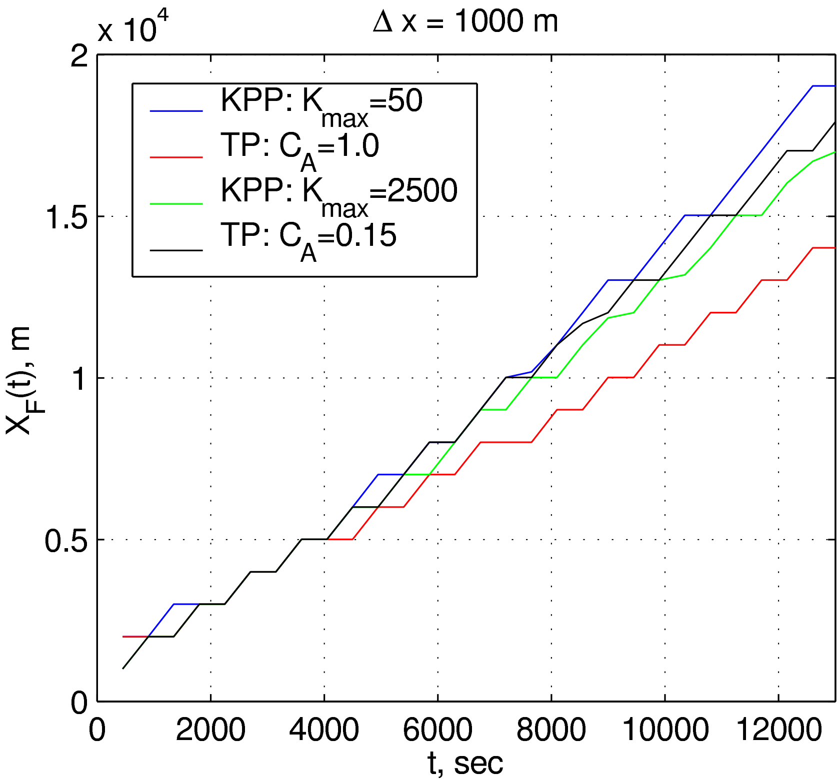


Figure 8: Position of the salinity front, $X_F$ (in m), as a function of time in HYCOM experiments with (a) $\Delta x = 1000$ m. Blue line: KPP with $K_{max} = 50\, cm^2 s^{-1}$, green: KPP with $K_{max} = 2500\, cm^2 s^{-1}$, red: TP with $C_A = 1.0$, and black: TP with $C_A = 0.15$.

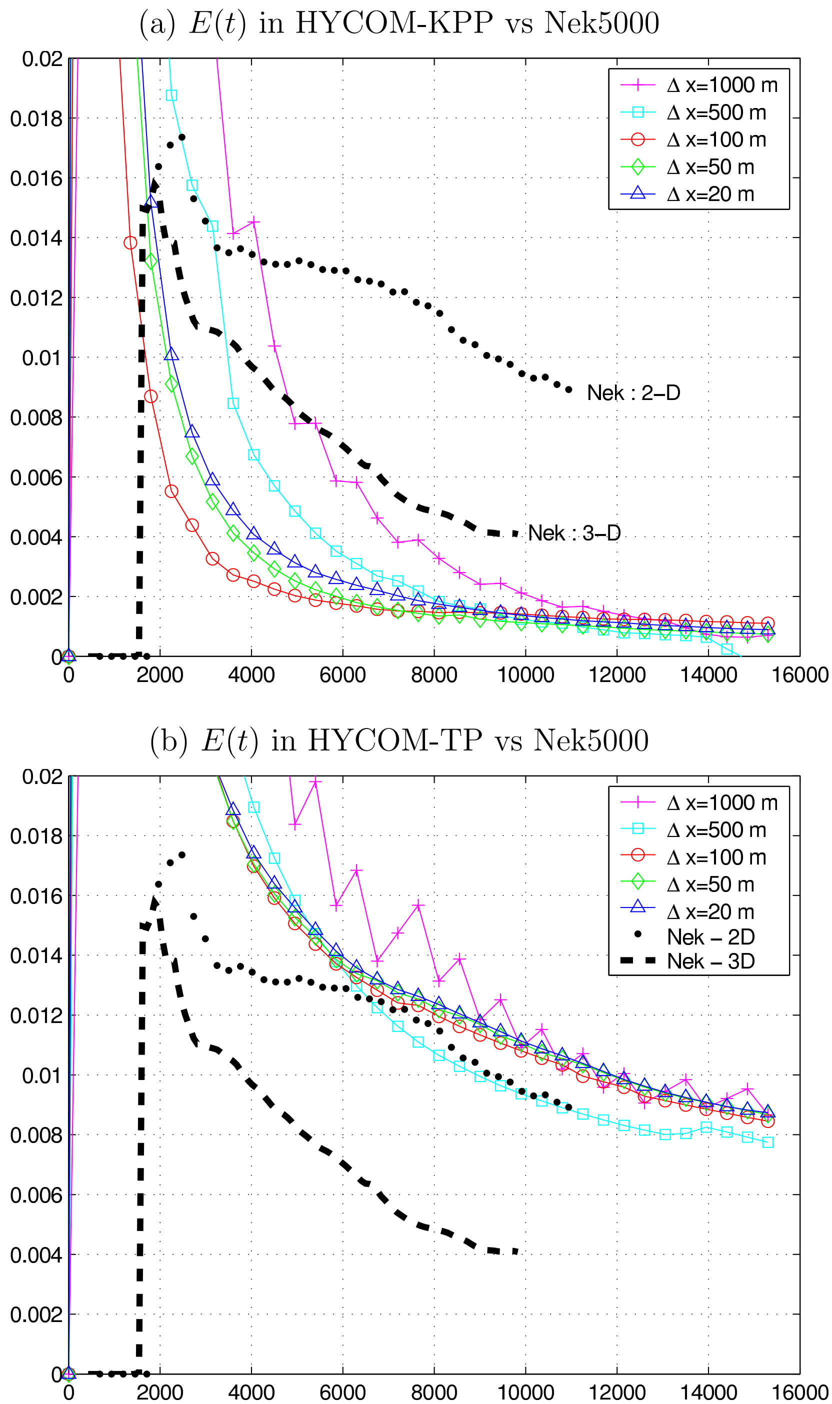


Figure 9: Time evolution of entrainment parameters, $E(t)$, in HYCOM experiments with (a) KPP and (b) TP at different horizontal grid spacings; crosses: $\Delta x = 1000m$, triangles: $\Delta x = 500m$, circles: $\Delta x = 100m$, diamonds: $\Delta x = 50m$, squares: $\Delta x = 20m$. Entrainment parameters from 2D and 3D nonhydrostatic experiments with Nek5000 are shown in the background, dotted: 2D, dashed: 3D.

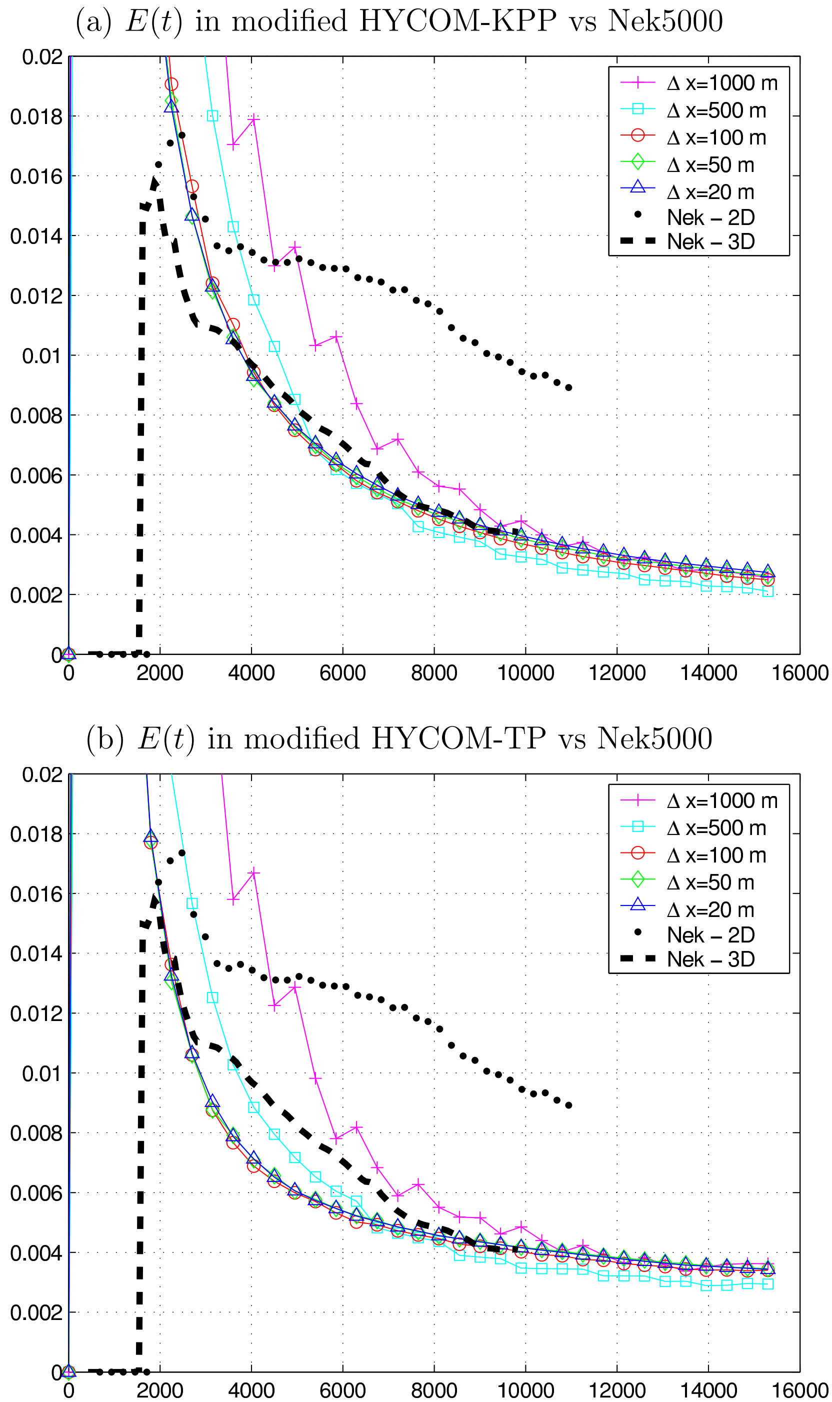


Figure 10: $E(t)$ in HYCOM experiments with (a) modified KPP ($K_{max} = 2500\, cm^2 s^{-1}$) and (b) modified TP ($C_A = 0.15$) at different horizontal grid spacings; crosses: $\Delta x = 1000m$, triangles: $\Delta x = 500m$, circles: $\Delta x = 100m$, diamonds: $\Delta x = 50m$, squares: $\Delta x = 20m$. Entrainment parameters from 2D and 3D nonhydrostatic experiments with Nek5000 are shown in the background, dotted: 2D, dashed: 3D.

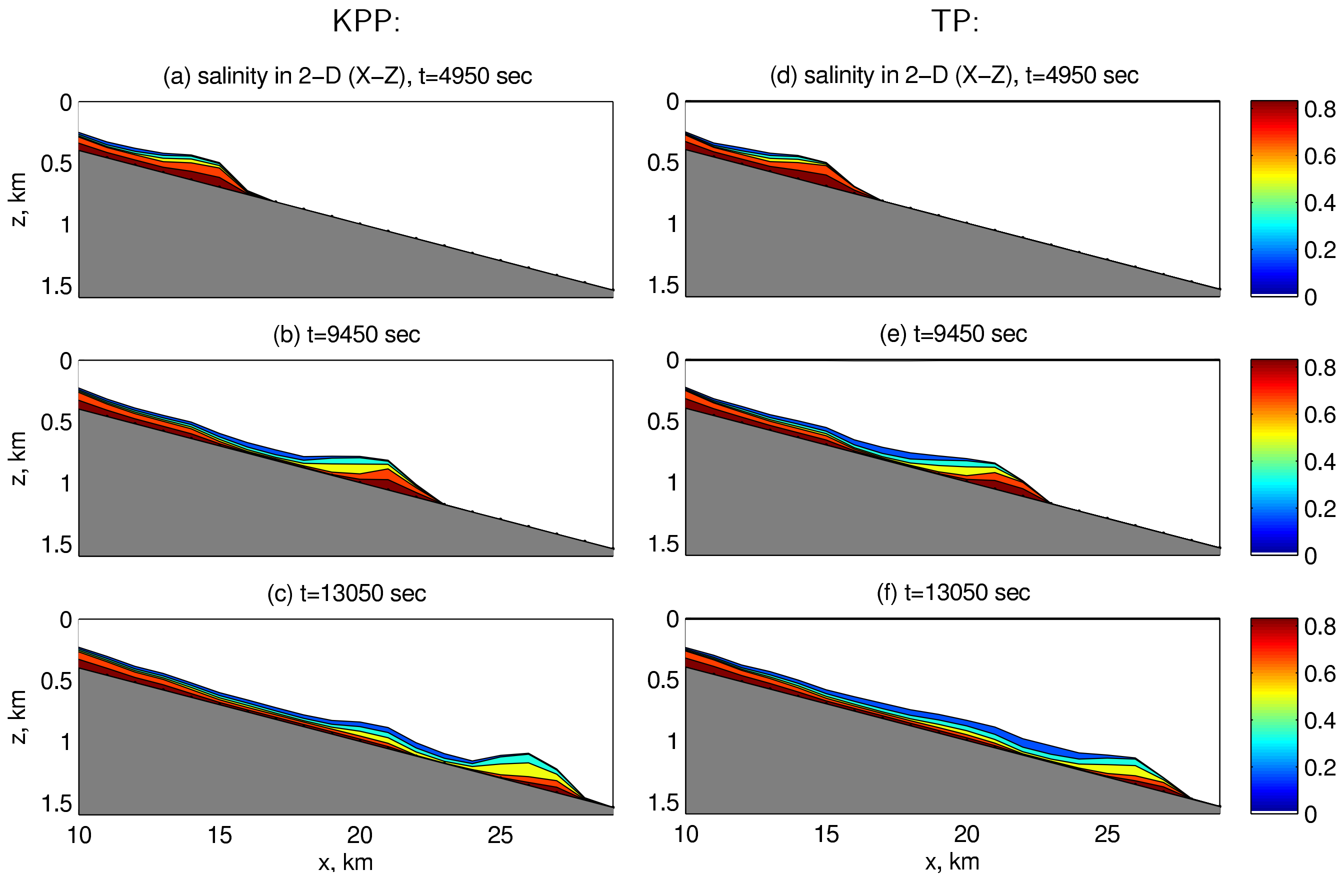


Figure 11: Evolution of salinity distribution in time in HYCOM experiments with modified parameterizations, (a) $t = 4960\,\mathrm{s}$, (b) $t = 9450\,\mathrm{s}$, and (c) $t = 13050\,\mathrm{s}$ using modified KPP ($K_{max} = 2500\,cm^2 s^{-1}$) with $\Delta x = 1000$ m, and (d), (e), (f) using modified TP ($C_A = 0.15$).

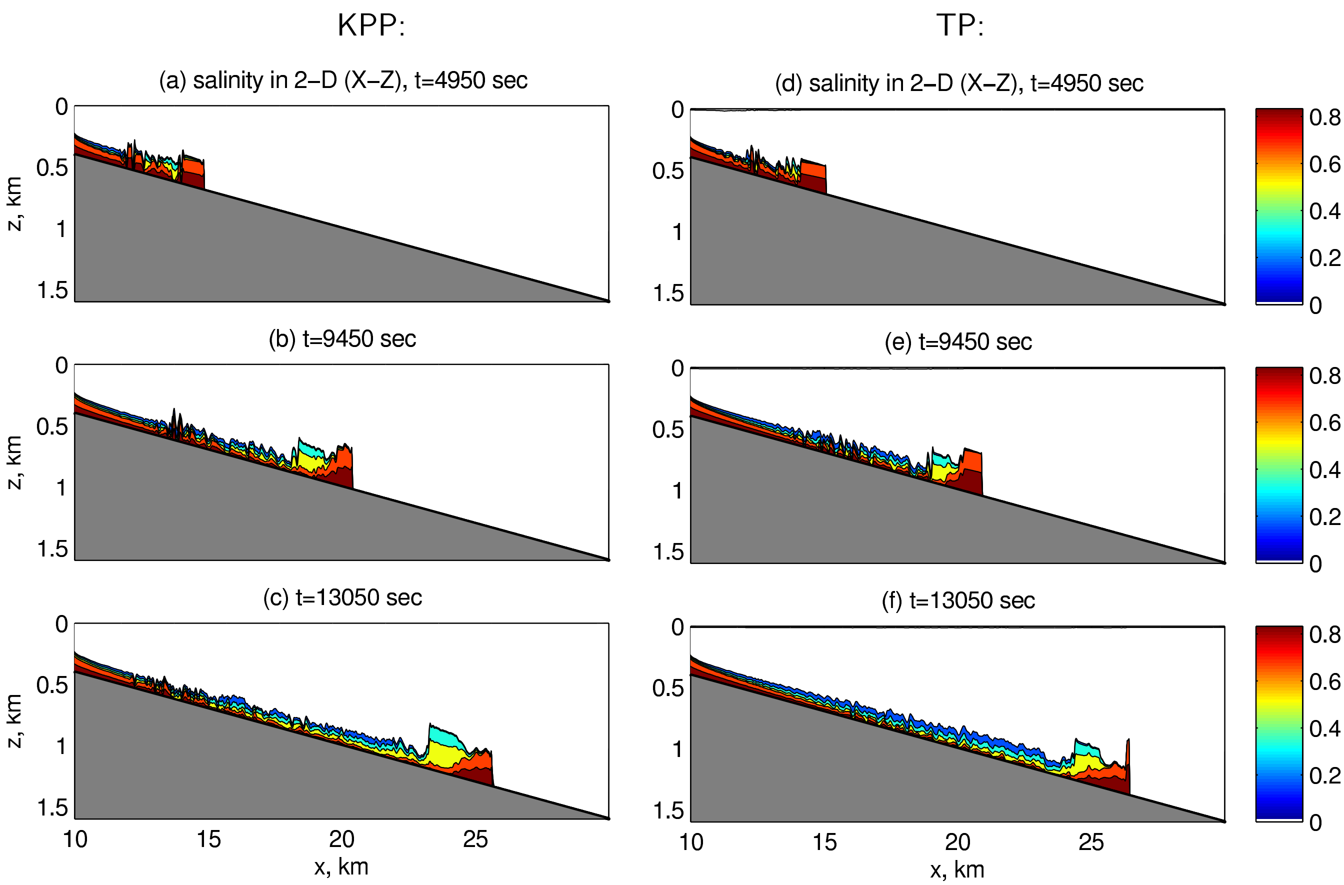


Figure 12: Evolution of salinity distribution in time in HYCOM experiments with modified parameterizations, (a) spanwise-average at $t = 4960\,\mathrm{s}$, (b) spanwise-average at $t = 9450\,\mathrm{s}$, and (c) spanwise-average at $t = 13050\,\mathrm{s}$ using modified KPP ($K_{max} = 2500\,cm^2 s^{-1}$) with $\Delta x = 20$ m, and (d), (e), (f) using modified TP ($C_A = 0.15$).

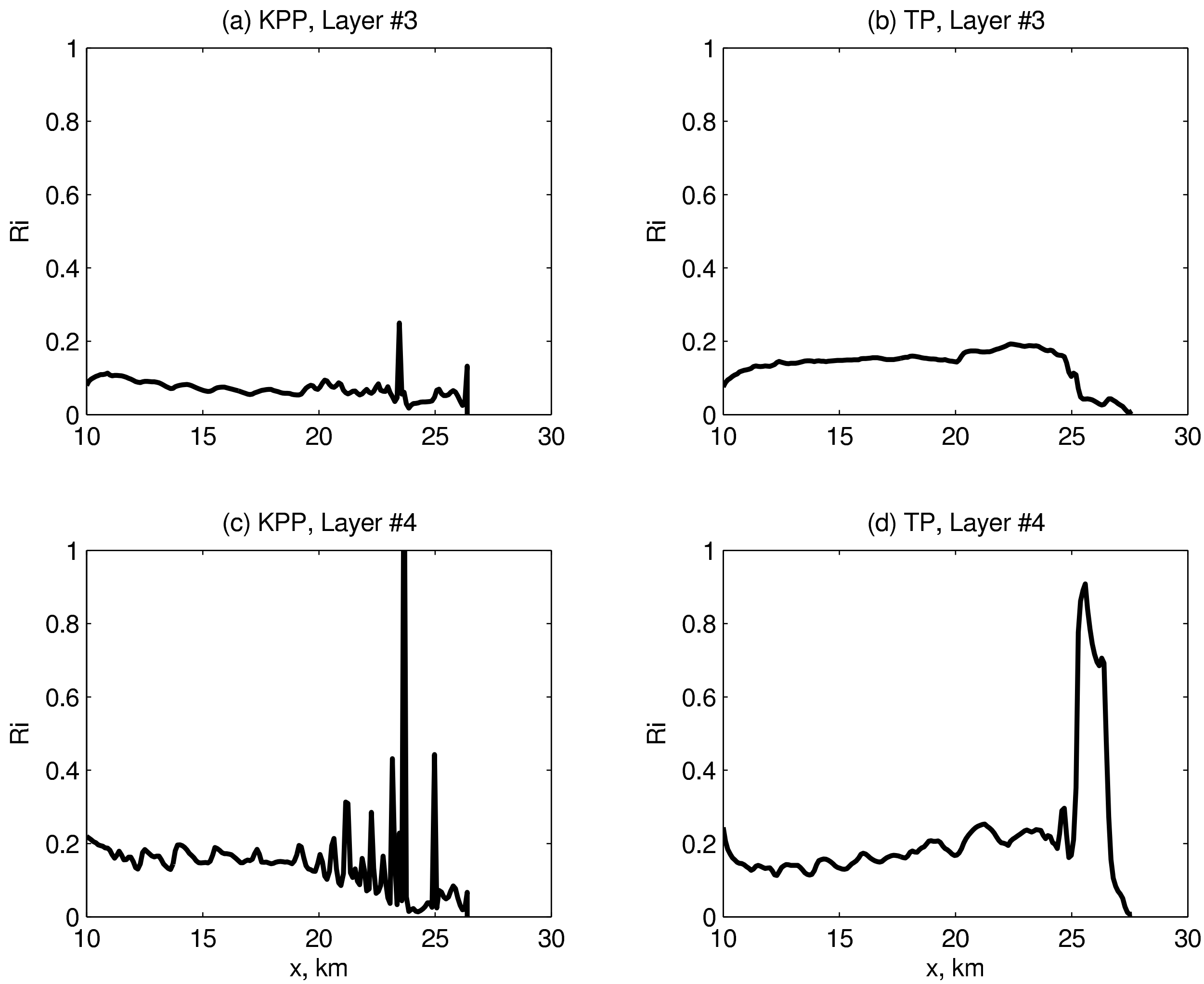


Figure 13: The distribution of $Ri$ along the flow direction averaged over the spanwise direction in the case of KPP in layers (a) 3 and (c) 4, and in the case of TP in layers (b) 3 and (d) 4, at the selected horizontal resolution of $\Delta x = 100\, m$ and at $t = 13050\, s$.

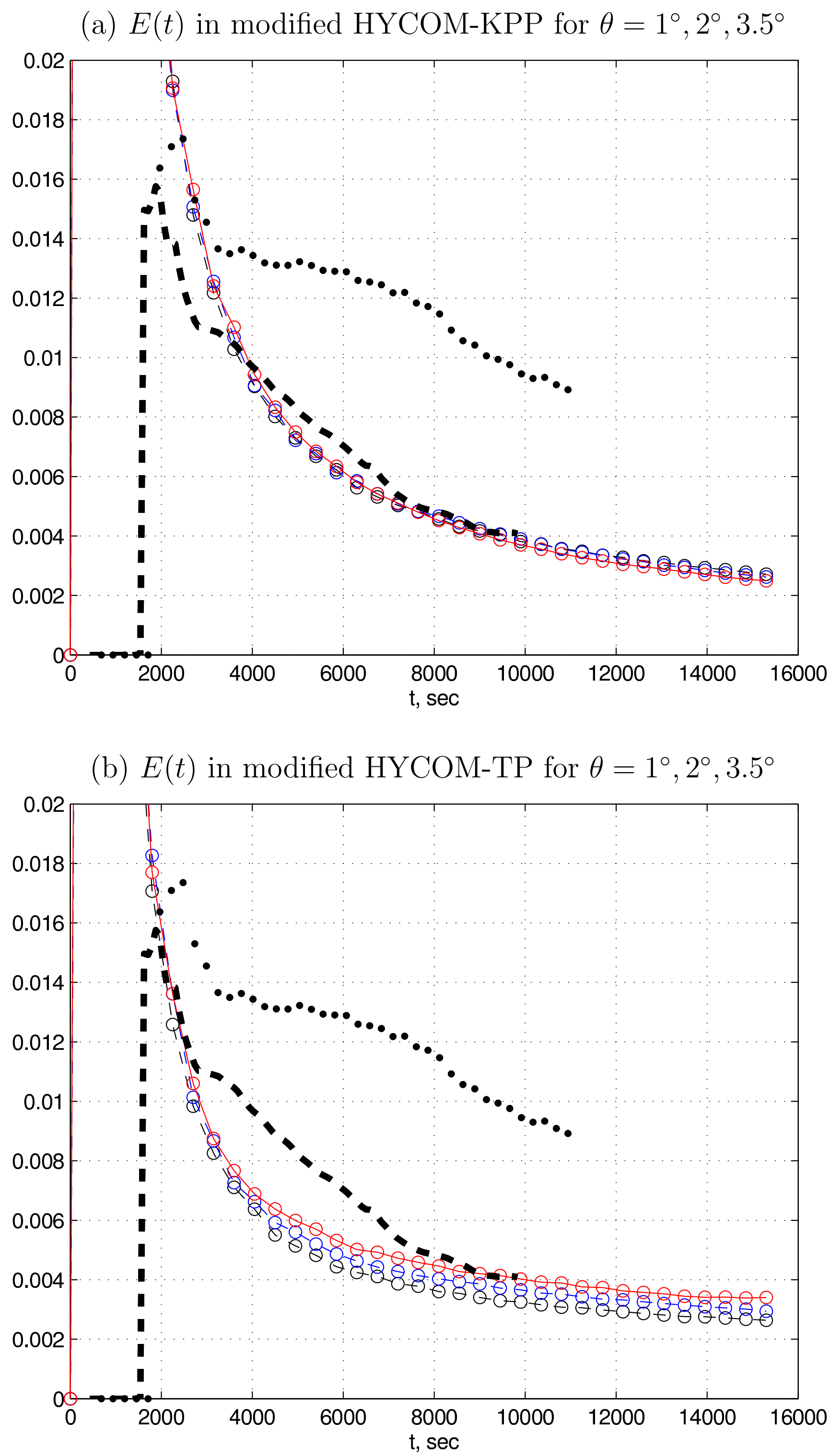


Figure 14: $E(t)$ in HYCOM experiments with (a) modified KPP ($K_{max} = 2500\,cm^2s^{-1}$) and (b) modified TP ($C_A = 0.15$) at $\Delta x = 100m$ for different slope angles $\theta = 1°$ (black lines), $\theta = 2°$ (blue lines), $\theta = 3.5°$ (red lines). Entrainment parameters from 2D and 3D nonhydrostatic experiments with Nek5000 are shown in the background, dotted: 2D, dashed: 3D.

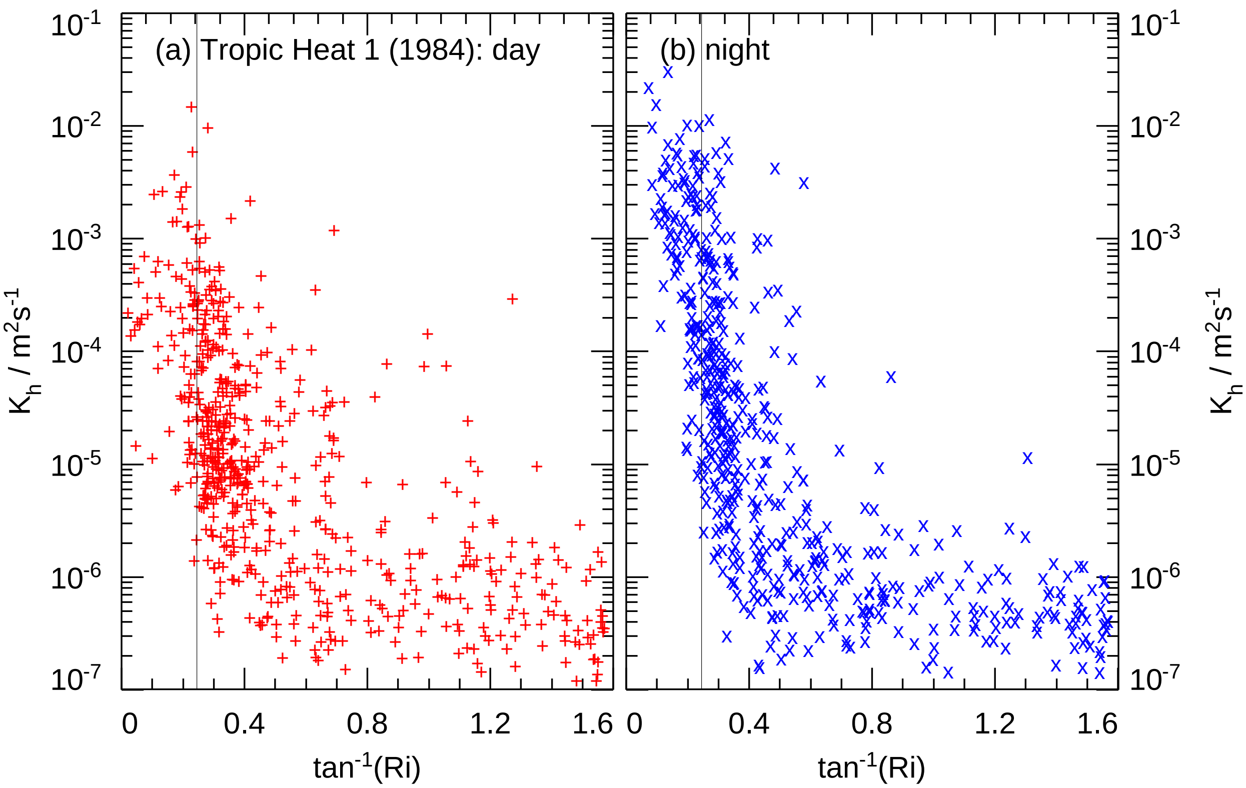


Figure 15: Hourly averages from the 1984 Tropic Heat 1 Experiment in the Pacific Equatorial Undercurrent at $0^o$, $140^o$W, eddy diffusivity of heat versus arc tangent of the local gradient Richardson number, (a) daytime data subject to oceanic heat gain and upper ocean stabilization, (b) nighttime data subject to oceanic heat loss and mixed layer convection. The data span the upper ∼150 m depth with the core of the Undercurrent and a minimum in shear near 110 m. Note that the shape of the data scatter changes little between daytime and nighttime, while more large $K_h$ appear at the high-$K_h$ end of the curve at night. The vertical lines in (a) and (b) indicate $Ri = 1/4$.